Simulation of Effects of Atmospheric Aerosols on Deep Turbulent Convective Clouds Using a Spectral Microphysics Mixed-Phase Cumulus Cloud Model. Part I: Model Description and Possible Applications

A. KHAIN, A. POKROVSKY, AND M. PINSKY

The Institute of Earth Sciences, The Hebrew University of Jerusalem, Givat Ram, Israel

A. SEIFERT

National Center for Atmospheric Research, Boulder, Colorado

V. PHILLIPS

Geophysical Fluid Dynamics Laboratory, Princeton, New Jersey

ABSTRACT

An updated version of the spectral (bin) microphysics cloud model developed at the Hebrew University of Jerusalem [the Hebrew University Cloud Model (HUCM)] is described. The model microphysics is based on the solution of the equation system for size distribution functions of cloud hydrometeors of seven types (water drops, plate-, columnar-, and branch-like ice crystals, aggregates, graupel, and hail/frozen drops) as well as for the size distribution function of aerosol particles playing the role of cloud condensational nuclei (CCN). Each size distribution function contains 33 mass bins.

The conditions allowing numerical reproduction of a narrow droplet spectrum up to the level of homogeneous freezing in deep convective clouds developed in smoky air are discussed and illustrated using as an example Rosenfeld and Woodley's case of deep Texas clouds.

The effects of breakup on precipitation are illustrated by the use of a new collisional breakup scheme. Variation of the microphysical structure of a melting layer is illustrated by using the novel melting procedure.

It is shown that an increase in the aerosol concentration leads to a decrease in precipitation from single clouds both under continental and maritime conditions. To provide similar precipitation, a cloud developed in smoky air should have a higher top height. The mechanisms are discussed through which aerosols decrease precipitation efficiency. It is shown that aerosols affect the vertical profile of the convective heating caused by latent heat release.

1. Introduction

Cloud–aerosol interaction is increasingly recognized as one of the key factors influencing the microphysical structure of clouds and precipitation regimes on local, meso-, and even global scales. The size and concentration of nucleated droplets depend on the concentration and size of aerosol particles (APs), serving as cloud condensation nuclei (CCN). Kaufman and Nakajima (1993) found a significant decrease in droplet size (from 15 to 9 μm) accompanied by an increase in drop concentration in continental clouds over the Amazon smoky area. Maritinsson et al. (1999) observed a significant increase in concentration (up to 2000 cm^{-3}), together with a substantial reduction of the effective droplet radius in polluted orographic clouds over a mountain ridge. The effects of aerosols on the droplet spectrum width have been presented recently by Andreae et al. (2003) in more detail.

The impact of aerosols on the rainfall is, supposedly, one of the most important issues of anthropogenic climate change (e.g., Hobbs 1993). Recent observations made with the Tropical Rainfall Measuring Mission (TRMM) satellite data demonstrated that the smoke from burning vegetation can practically shut off warm rain formation in tropical clouds (Rosenfeld 1999). Rosenfeld and Woodley (1999) observed that in polluted areas over Thailand and Indonesia, smoky clouds do not precipitate at all because of the narrow spectra of small droplets. At the same time, similar clouds begin precipitating in clear air in 20–25 min after their formation. A decrease in precipitation in urban areas was reported

Corresponding author address: Prof. Alexander Khain, The Institute of Earth Sciences, The Hebrew University of Jerusalem, Givat Ram 91904, Israel.
E-mail: Khain@vms.huji.ac.il

(Rosenfeld 2000). It is well known that continental and maritime clouds differ both microphysically and dynamically. The question arises—to what extent is this difference related to the properties of APs over oceans and continents?

Note that the reduction of warm rain production rate in cumulus clouds growing in smoky air does not mean that the accumulated precipitation will automatically decrease too. A decrease in warm rain production may, for instance, result in an increase in precipitation formed by cloud ice melting. Recall in this connection that, according to the glaciogenic cloud seeding hypothesis, additional ice production results in a higher total precipitation amount, owing to a more effective diffusion growth of cloud ice, compared to water drops.

One of potentially efficient methods to investigate aerosol effects on precipitation formation is the utilization of advanced spectral bin microphysical (SBM) cloud models. Many SBM models are warm rain models (e.g., Clark 1973, 1976; Kogan 1991; Stevens et al. 1996; Pinsky and Khain 2002). Several SBM models use one size distribution function to describe cloud ice (e.g., Khvorostyanov et al. 1989; Hall 1980; Khain et al. 1993; Ovtchinnikov and Kogan 2000). In this approach, the categories with the smallest masses are interpreted as ice crystals, while larger ice particles are usually considered as graupel. There are only a few models of mixed-phase clouds with a detailed description of cloud ice. These models have several size distribution functions for different types of cloud ice (Takahashi 1976; Khain et al. 1996, 1999, 2000; Reisin et al. 1996a,b; Levin et al. 1998; Yin et al. 2000a,b; Rasmussen et al. 2002). These mixed-phase cloud microphysical models have a high potential to provide more accurate simulations of precipitation formation and simulations of cloud–aerosol interactions than those models with simpler ice schemes.

Advanced SBM schemes include the budget of atmospheric aerosols (e.g., Flossman et al. 1985; Kogan 1991; Khain and Sednev 1996; Khain et al. 1999, 2000; Yin et al. 2000a,b). The APs are described by a special size distribution that changes as a result of advection and activation (droplet nucleation). The values of supersaturation are used to determine the sizes of APs to be activated and the corresponding sizes of newly nucleated cloud droplets.

The spectral (bin) microphysical cloud models were successfully used for the investigation of separate microphysical processes (e.g., Takahashi 1976; Tzivion et al. 1989; Reisin et al. 1996b; Ovtchinnikov and Kogan 2000; Ovtchinnikov et al. 2000), effects of cloud microphysics on spatial redistribution of precipitation in the coastal zones (e.g., Khain et al. 1993; Khain and Sednev 1996), simulation of stratiform clouds and their radiative effects (e.g., Liu and Kogan 1998; Rasmussen et al. 2002), simulation of cloud seeding (e.g., Khvorostyanov et al. 1989; Reisin et al. 1996c; Yin et al.

2000b), and cloud chemistry (e.g., Flossman et al. 1985), etc.

At the same time, the number of studies in which SBM models are used for the investigation of aerosol effects on precipitation from mixed-phase clouds is quite limited. Yin et al. (2000b) studied the role of giant CCN on precipitation. A decrease in the rate of warm rain production in deep cumulus clouds with an increase in the CCN concentration has been clearly demonstrated by Khain et al. (1999) using the SBM Hebrew University Cloud Model (HUCM). A substantial improvement in the understanding of many aspects of microphysics, as well as in the formulation of mathematical microphysical algorithms, has been attained in the last few years. Khain et al. (2001b) reported the first results of simulation of the microphysical structure of deep growing Texas convective clouds (Rosenfeld and Woodley 2000).

Note that because of computer limitations most mixed-phase SBM models are two-dimensional. Three-dimensional SBM models are either warm rain microphysical models or contain only one size distribution of description of wide variability of cloud ice. Besides, the computational region used in these 3D models allows simulations of only single clouds. A novel 3D SBM mesoscale model has been recently developed by the implementation of the updated HUCM microphysics into the fifth-generation Pennsylvania State University–National Center for Atmospheric Research (PSU–NCAR) Mesoscale Model (MM5) dynamical framework (Lynn et al. 2005a,b). Simulations of a rain event over Florida accompanied by a squall line formation showed that the new model drastically improved the precision in the reproduction of the precipitation rate and amount. The updated version of the spectral microphysics used in the 3D SBM mesoscale model differs substantially from that described by Khain and Sednev (1996).

The structure of Part I of this study is the following: We describe the microphysical scheme in section 2, focusing on the new implementations. The results of several sensitivity experiments are discussed (section 3), then we illustrate some approaches allowing the reproduction of narrow droplet spectra in deep continental convective clouds up to levels as high as 9.5 km. Section 4 presents different examples of aerosol effects on cloud microphysics and thermodynamics to be investigated in more detail in successive studies, and the mechanism through which atmospheric aerosols decrease precipitation efficiency is described. Section 5 provides a summary of Part I.

2. The model description

Some elements of the HUCM dynamics and microphysics are described in Khain and Sednev (1996) and are briefly summarized below. New improvements are described in more detail. The model is two-dimensional and nonhydrostatic; the equations for the velocity com-
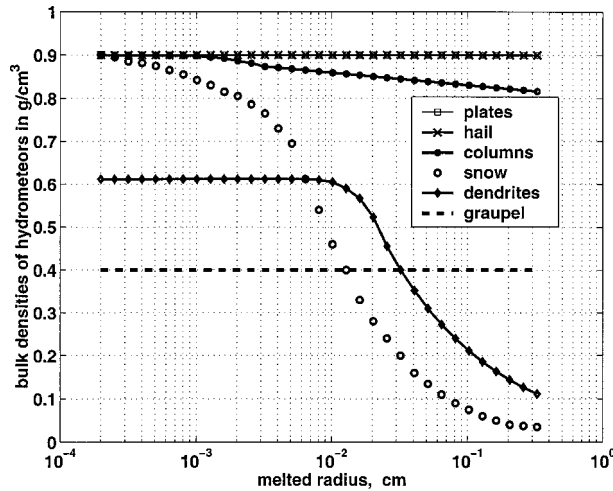
FIG. 1. Bulk densities of different hydrometeors as the function of their melted radii.
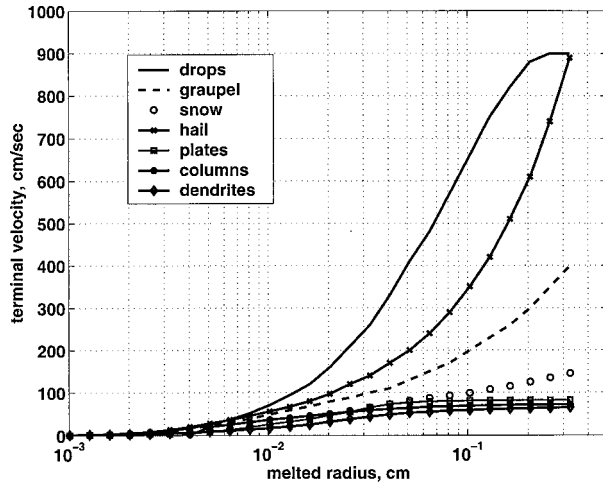

FIG. 2. Terminal fall velocities of different hydrometeors as the function of their melted radii.

ponents u and $w,$ as well as the continuity equation, were reduced to the equations for the vorticity and the streamfunction. Thermodynamic equations include the equation for the potential temperature θ and the water vapor–dry air mixing ratio q.

a. Size distributions of atmospheric particles

The model microphysics is based on solving an equation system for size (number) distribution functions $f_i(\mathbf{x}, m, t)$ ($i = 1$, water drops; 2–4, ice crystals; 5, aggregates; 6, graupel; 7, frozen drops/hail; and 8, CCN) represented by 33 mass doubling categories (bins). Columnar, plate-like, and dendrite crystals are chosen to represent a variety of ice crystal types. Characteristics of these ice crystals (mass, the diameter-to-thickness ratio or the diameter-to-length ratio, and bulk density) are taken mainly from Magono and Lee (1966) and Pruppacher and Klett (1997). Dependencies of the bulk densities of cloud hydrometers used in the HUCM on their melted radii are shown in Fig. 1. The fall velocities of water drops and graupel are calculated following Beard (1976) and Khain et al. (2001a), respectively. The dependencies of the terminal velocities of ice crystals and snowflakes on their size, taken mainly from Pruppacher and Klett (1997), are valid within certain ranges of particle sizes. To provide reasonable values beyond these ranges, we properly extrapolated the fall velocities for small ice crystals. The applied dependencies of hydrometeors' fall velocities at the 1000-mb level on melted radii are presented in Fig. 2. We believe that the ranges of both bulk densities and terminal velocities used are wide enough to represent the essential variations of ice in clouds.

The mass grids used for hydrometeors of all types are similar. This simplifies the calculation of interaction between hydrometeors of different bulk densities. In the current model version, the maximum mass of dry aero-

sol particles (CCN) corresponds to the mass of the smallest 2-μm-radius droplets. The size distribution function f_{ik} of a kth mass category is described as follows:

$$
\frac{\partial f_{ik}}{\partial t} + \frac{\partial u f_{ik}}{\partial x} + \frac{\partial (w - V_{tik}) f_{ik}}{\partial z}
$$

$$
= \left(\frac{\partial f_{ik}}{\partial t}\right)_{\text{nucl}} + \left(\frac{\partial f_{ik}}{\partial t}\right)_{\text{c/e}} + \left(\frac{\partial f_{ik}}{\partial t}\right)_{\text{d/s}} + \left(\frac{\partial f_{ik}}{\partial t}\right)_{\text{col}}
$$

$$
+ \left(\frac{\partial f_{ik}}{\partial t}\right)_{\text{f/m}} + \left(\frac{\partial f_{ik}}{\partial t}\right)_{\text{break}}, \tag{1}
$$

where V_{tik} is the terminal velocity of hydrometeors of type i belonging to the kth mass bin, the terms on the right-hand side represent the rates of the size distribution function change due to nucleation, condensation/evaporation of drops, deposition/sublimation of ice particles, collisions, freezing/melting, and breakup, respectively.

Advection of size distributions and other variables, as well as freezing/melting and collisions, are calculated with a "dynamical" time step Δt_{dyn} (usually 5–10 s). Nucleation of droplets and ice crystals is calculated using time step Δt_{nucl}, which is several times smaller than the dynamical time step. Diffusion growth/evaporation of droplets and ice particles is calculated using the variable microphysical time step Δt_{diff}, whose magnitude is calculated as discussed below. The time steps are chosen so that their further decrease does not lead to any significant change of the results.

b. Nucleation of droplets and ice particles

For the calculation of the initial (at $t = 0$) CCN size distribution, an empirical dependence $N(S_w)$ is used, where S_w is the supersaturation with respect to water. In particular, the dependence in the form

$$N = N_o S_w^k \qquad (2)$$

can be used (Pruppacher and Klett 1997). In (2), N_o and k are measured constants. We use different magnitudes of N_o and k within different ranges of supersaturations (or the ranges of CCN size). The procedure of the calculation of size of nucleated droplets is described by Khain et al. (2000). At $t > 0$, the prognostic equation (1) for nonactivated CCN size distribution is solved. At each time step a value of S_w is calculated in all grid points. Using the value of S_w, a critical CCN radius is calculated according to the Kohler theory. CCNs with radii exceeding the critical value are activated (new droplets are nucleated). Corresponding bins of the CCN size distributions become empty. As a result of droplet nucleation, the concentration of aerosols (CCN) in the convective zone decreases.

Nucleation of ice crystals is described following the formula presented by Meyers et al. (1992) relating the number concentration of deposition and condensation-freezing ice nuclei (IN), N_d, to supersaturation with respect to ice, S_{ice},

$$N_d = N_{do} \exp(a_d + b_d S_{ice}), \qquad (3)$$

where $N_{do} = 10^{-3}$ m^{-3}, $a_d = -0.639$, and $b_d = 12.96$. Nucleation is prevented for temperatures warmer than $-5°$C. In case $S_{ice} > 25\%$, it is assumed equal to 25%, as concerns the utilization of (3). Formula (3) actually provides the distribution of a number of active IN with respect to supersaturation S_{ice}. The number of newly activated ice crystals at each time step in a certain grid point, dN_d, is calculated as follows:

$$dN_d = \begin{cases} b_d N_d dS_{ice}, & \text{if } dS_{ice} > 0 \\ 0, & \text{if } dS_{ice} < 0, \end{cases} \qquad (4)$$

where $dS_{ice} = [\partial S_{ice}/\partial t + u(\partial S_{ice}/\partial x) + w(\partial S_{ice}/\partial z)]dt$.

We believe that this semi-Lagrangian approach expressed by (4) is a natural physical approach, corresponding to the logic of the physical process. According to Takahashi et al. (1991), the temperature-dependent nucleation proceeds as follows: plate-like crystals form at $-8 > T_c \geq -14°$C and $-18 > T_c \geq -22.4°$C, columnar crystals arise at $-4 > T_c \geq -8°$C, $T_c < -22.4°$C, and dendrites (branch-type crystals) form at $-14 > T_c \geq -18°$C.

Secondary ice crystal production is treated according to the results of Hallett and Mossop (1974) and Mossop and Hallett (1974). At $-5°$C, one splinter (an ice crystal of the smallest resolvable size) is created per 200 droplets, with the diameter over 24 μm collected by riming graupel or hail. This maximum splinter production rate decreases toward the ends of the temperature range, which are set at $-3°$ and $-8°$C, respectively. The splinters are assigned to plate-type ice crystals with the density of 0.9 g cm^{-3}.

c. Immersion freezing

Immersion freezing is parameterized by using the singular hypothesis (Vali 1994), according to which the number of frozen drops does not change with time for a given supercooling. It is assumed that immersion nuclei are distributed homogeneously throughout liquid cloud water and that their activity increases when the temperature decreases. Following Ovtchinnikov and Kogan (2000), we use the temperature dependence of immersion nuclei given by Vali (1975):

$$N_{im} = N_{imo}(-0.1\ T_c)^{\gamma}, \qquad (5)$$

where N_{im} is the number of active immersion nuclei per unit volume of liquid water, $N_{im} = 10^7$ m^{-3}, and $\gamma = 4.4$ for cumulus clouds. The number of activated immersion IN per unit volume of a cloud parcel when its temperature decreases by dT_c is calculated as $dN_{im} = -10^{-\gamma} N_{imo} \gamma T_c^{\gamma-1} dT_c$, where dT_c is calculated similar to dS_{ice} in (4). Assuming that activation of only one immersion IN within a drop is enough to freeze it, we redistributed the number of activated IN between mass categories. The change of drop size distribution function f_{1k} of the kth mass category by immersion freezing is expressed as

$$(df_{1k})_{freez} = -\frac{4}{3}\pi r_k^3 f_{1k} dN_{im}. \qquad (6)$$

Frozen droplets with the radii under 100 μm are assigned to plate crystals (whose density is 0.9 g cm^{-3}). Larger droplets are assigned to hail/frozen drops particles.

d. Melting procedure

A new *melting* procedure has been implemented in the HUCM, by extending the scheme applied by Phillips et al. (2003). The procedure takes into account processes of diffusion of heat into the melting particles and the modification of the terminal velocity of particles during melting, as well as the shedding of water in case the mass of water exceeds a certain threshold. In this procedure, the representation of melting is based partly on the models by Rasmussen et al. (1984a) and Rasmussen and Heymsfield (1987) for graupel/hail and by Mitra et al. (1990) for crystals/snow. The fundamental concept in this procedure is that meltwater initially accumulates in the interior of the ice particle, soaking up air spaces (except for particles with a bulk density > 910 kg m^{-3}). When all air spaces are filled up, meltwater begins to accumulate on the exterior of the particle. Shedding of raindrops occurs when the meltwater mass on the exterior of the particle exceeds a critical equilibrium value that depends on the mass of the ice particle. Shed drops have a size that is dependent on the Reynolds number (Rasmussen et al. 1984b). The heat budget of the particle determines its melting rate and includes diffusion of heat and (vapor) mass to and from the particle, with latent

cooling from evaporation of meltwater. For Reynolds numbers < 3000, circulation of the meltwater is assumed to occur, and the ice core is embedded in a spherical shell of meltwater. At higher Reynolds numbers, circulation of meltwater does not occur due to the oblate shape of the particle (Mason 1956). For the largest hail (Reynolds numbers > 20 000), the heat transfer coefficient for rough spheres is applied (Bailey and Macklin 1968).

Snowflakes and crystals are assumed to have an ice skeleton structure that is incollapsible but of varying axial ratio during melting. Their capacitance and axial ratio are interpolated with respect to liquid fraction toward "totally melted" values of 80% of the dry value and 0.3, respectively. Empirical functions for the capacitance and axial ratio of dry ice particles are those given by Pruppacher and Klett (1997) for columns, dendrites, plates, and snow. Whereas for snow and crystals there is a monotonic increase of the terminal velocity with liquid fraction during melting, the situation is more complex for hail and graupel. At the onset of melting, hail and graupel with Reynolds numbers < 4000 experience a sudden increase in terminal velocity because the drag coefficient becomes that of a smooth sphere as the ice surface becomes wet. However, after the ice particle is fully soaked with meltwater, the shape of the particle is affected by meltwater being aerodynamically molded. A torus of water builds up near the equator of the ice sphere, increasing the particle's cross-sectional area and decreasing its terminal velocity. During the accumulation of meltwater on the exterior of the ice particle, there is a linear interpolation of the terminal velocity between the "just soaked" value and the value corresponding to a critical equilibrium mass of meltwater. This interpolation is based on the fraction of water on the surface compared to the equilibrium amount.

To describe the melting process, a melted (liquid) fraction in each mass bin of ice particles is calculated and advected along with the particles. As soon as the liquid fraction in a particular bin exceeds 0.99, the particles belonging to the bin are assigned to liquid droplets of a corresponding mass. If partially melted particles cross the freezing level in updrafts, they freeze again, and the liquid fraction is set equal to zero.

e. Diffusion growth/evaporation of liquid drops and deposition/sublimation of ice particles

Diffusion growth/evaporation of liquid drops and deposition/sublimation of ice particles of mass m_{ik} (i is the type of hydrometeor, k is the number of the mass category) by water vapor deposition/sublimation is expressed as follows (Pruppacher and Klett 1997):

$$\frac{dm_{ik}}{dt} = F_{ik}S_{w/ice}, \qquad F_{ik} = \frac{4\pi C_{ik}}{G_i}, \qquad (7)$$

where $G_i = R_v T/e_{w/ice} D_v + (L_{w/ice}/k_a T)(L_{w/ice}/R_v T - 1)$, $e_{w/ice}$ is the saturated water vapor pressure with respect to water or ice, and $L_{w/ice}$ is the specific latent heat with respect to water or ice, respectively. Here, D_v, k_a, and R_v are the water and air diffusivity coefficients and the moist air gas constant, respectively. Expressions for the "electrostatic capacitance" of particles of different shape C_{ik} are taken from (Pruppacher and Klett 1997).

Supersaturations with respect to water and ice are calculated analytically by solving the equation system for supersaturations with respect to water and ice, and Eq. (7) at each time step Δt_{diff} (Tzivion et al. 1989; Khain and Sednev 1996). Time steps Δt_{diff} are chosen equal to the time needed for particles belonging to the smallest nonempty bin to reach the next mass category, in case of condensation/deposition, or to be transferred to a neighboring smaller mass bin, in case of evaporation/sublimation. This choice of Δt_{diff} is used to ensure constant values of coefficients in the differential equations for supersaturations. At each nth time step $\Delta t_{diff,n}$, the change of the droplet/ice particle mass is analytically calculated as $F_{ik} \int_{t_n}^{t_n + \Delta t_{diff,n}} S_{w/ice} \, d\tau$. The final particle mass at $t + \Delta t_{dyn}$ is calculated as

$$m_{ik}^{t+\Delta t_{dyn}} = m_{ik}^t + F_{ik} \int_{t_n}^{t+\Delta t_{dyn}} S_{w/ice} \, d\tau, \qquad (8)$$

where $\int_{t_n}^{t+\Delta t_{dyn}} S_{w/ice} \, d\tau = \Sigma_n \int_{t_n}^{t_n + \Delta t_{diff,n}} S_{w/ice} \, d\tau$. This approach takes into account the changes of supersaturation during one microphysical time step, which, as it was found in supplemental experiments, is of high importance for the precise simulation of size spectra evolution. To calculate new values of distribution functions, the new spectrum has to be remapped into a specified mass grid (e.g., Kovertz and Olund 1969) that usually leads to the artificial formation of larger drops at each time step. To decrease the number of remapping, the calculation of new size distribution functions in the new model version is conducted only at the end of the dynamical time step Δt_{dyn}, which leads to a 10–15-min time delay in raindrop formation in simulations of continental clouds, compared to the case when the remapping is conducted at each of $\Delta t_{diff,n}$ steps.

f. Drop and ice collisions

The process of drop and ice collisions is described by solving the stochastic kinetic equation of collisions. The values of the drop–drop collision efficiencies obtained by different authors are often inconsistent (Pruppacher and Klett 1997). Pinsky et al. (2001) recalculated the collision efficiencies and collision kernels for drops within a wide range of sizes from 1 to 300 μm with a high resolution of 1 μm. The calculations were conducted for several pressure levels: 1000, 750, and 500 hPa. It was found that the collision efficiency and the collision kernels significantly increase with height. The increase is related to the decrease in the air density and the corresponding increase in relative velocities between colliding droplets. For certain drop pairs, the collision

efficiency at 500 hPa was found to be twice as large as at 1000 hPa. These new tables of collision efficiencies were implemented into the HUCM. In case the computational level is located between these three pressure levels, the collision efficiencies were found by the interpolation. The collision efficiencies above the 500-hPa level are assumed to be equal to those at 500 hPa. In this way, the dependence of collision rate upon the height has been taken into account.

The process of water–ice and ice–ice collisions is described by a system of stochastic kinetic equations for all types of cloud hydrometeors. The precise and computationally efficient method of Bott (1998) for solving the stochastic equation for drop collisions has been extended to water–ice and ice–ice collisions. These collisions lead to the formation of particles belonging to different types. The following ''rules'' have been assumed to apply to particles' transformation by collisions: 1) drop–drop collisions: new particles are water drops; 2) drop–crystal collisions and drop–snowflake (aggregates') collisions: if the mass of drops is less than that of crystals/snowflakes, new ice crystals/snowflakes are formed; otherwise either graupel or hail is formed depending on the air temperature; 3) drop–graupel collisions: either graupel or hail is formed depending on the air temperature; 4) drop–hail collisions: the result is hailstone formation; and 5) ice crystal–ice crystal, crystal–snowflake, and snowflake–snowflake collisions: snowflakes are formed.

The rules listed above, according to which particles formed by collisions are assigned to various hydrometeor types, are valid only for single acts of particle collisions. Continuous utilization of these rules for drop–ice collisions may lead to artifacts. For instance, a large ice crystal can sequentially collect small water drops and still remain an ice crystal. Actually, after a significant number of collisions with drops, the crystal should be assigned to graupel. In the HUCM it is assumed that riming of ice crystals and snowflakes leads to graupel formation if the mass of the rimed fraction exceeds half of the particle mass, and the melted radius of the resulting particle exceeds 100 μm. Since the ice particle memory of the rimed fraction is not stored in the model, the transformation of ice particles into graupel by riming is conducted as follows. As was mentioned above, the model uses a mass grid, in which the mass of each subsequent bin is twice as large as that of the previous one. The coalescence of drops of mass i and ice crystals of mass $j > i$ leads on this grid to the formation of rimed particles whose mass is located in between the masses of bins j and $j + 1$. These particles should be separated between the two bins of the regular mass grid. Since the particles to be put into bin $j + 1$ have a mass twice as large as those to be put into bin j, one can assume that they contain a riming fraction equal to or larger than 50%. Therefore, these particles were assigned to the graupel category. The particles

remaining in bin j were assigned either to the ice crystal or snowflake categories.

When ice–water drop collisions are being considered, one has to distinguish between the cases when ice particles serve as collectors of small droplets and when large drops collect ice particles. We assume that ice crystals serve as collectors if their mass is larger than that of collected drops. Crystal–drop collision efficiencies in this case were set according to Ji and Wang (1990), Wang and Ji (1997), and Pruppacher and Klett (1997). A specific feature of these collisions is the existence of a cutoff size of ice crystals, below which the crystals are unable to collect droplets. This size is about 100 μm for plates and about 50 μm for columnar crystals, respectively (Pruppacher and Klett 1997).

The efficiency of snowflake–droplet collisions and coalescence is not well known. It is greatly affected by porous effects, which depend on the snowflake structure, temperature, and other parameters. Porous effects seem to increase the coalescence efficiency of snowflakes by an order of magnitude, compared to those of solid discs (Lew et al. 1986a,b; Matsuno 1987; Pruppacher and Klett 1997). We assume that the collision efficiency between droplets and snowflakes are higher than that of plate-like crystals–droplets by a factor of 10, not exceeding, however, 1.

There are only a few studies in which the collision efficiencies between drops of several hundred microns in radius and plate-like and columnar crystals are presented (Lew and Pruppacher 1983; Lew et al. 1985). We interpolated/extrapolated the available data to calculate the table of collision efficiencies required. Large drop–snowflake collision efficiencies turn out to be equal to 1 due to the large sizes of these colliding particles.

Detailed hydrodynamical calculations of graupel–drop collision efficiencies have been conducted by Khain et al. (2001a). Figure 3 presents, as an example, the graupel–water collision efficiencies for 0.4 g cm^{-3} graupel density. One can see that the difference between graupel–drop and drop–drop collision efficiencies is especially significant for small graupel and small droplets. For instance, graupel particles with radii below 100 μm are unable to collect droplets with radii below 8 μm. As soon as the drop terminal velocity becomes higher than that of graupel (so water drops capture graupel), the collision efficiency experiences a jump to values significantly higher than 1 and then decreases quickly to about 1 with an increase in the drop size. The graupel–water collision kernels calculated in this way were used in the updated version of the HUCM.

g. Turbulence effects on collisions

In spite of a significant uncertainty with regard to turbulence/inertia effects, theoretical and laboratory results indicate that the rate of collisions in turbulent flows can be significantly (several times) higher than in calm
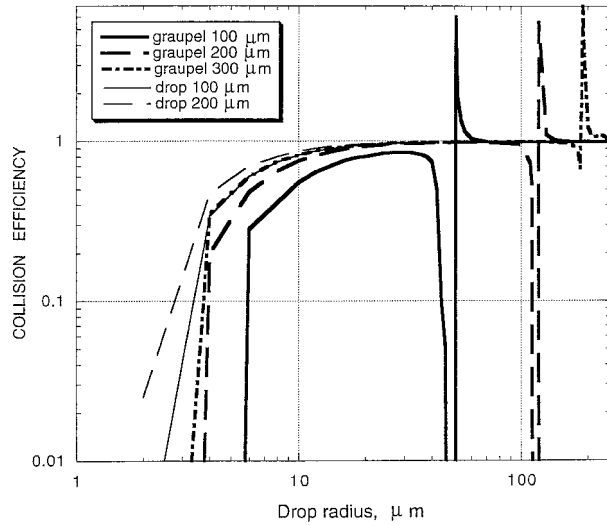
FIG. 3. Graupel–water collision efficiencies for 0.4 g cm^{-3} graupel density at 750 hPa.

air. Turbulence effects on drop–drop collision kernels are taken into account proceeding from the evaluations made in the studies by Pinsky et al. (1999, 2000). In turbulent flows, the collision rate depends on the size of colliding droplets and on turbulence intensity, and is evaluated as 1.5–6.0 times higher than those in the pure gravity case. The collision kernel for a droplet pair containing large droplets (with radii over 20 μm) increases in a turbulent flow mainly due to an increase in the swept volume, which can amount to 10%–30% depending on the drop size and turbulence intensity. According to Pinsky and Khain (1998) and Pinsky et al. (1998), the graupel–drop collision kernels for middle-density graupel with radii ranging from 100–500 μm

are significantly larger in the case of high intensity turbulence, compared to the pure gravity case.

To take into account the effects of turbulence, the gravity height-dependent collision kernels were multiplied by certain factors based on the results of the studies mentioned above. Using the results of turbulent velocity fluctuation measurements in cumulus clouds (Mazin et al. 1989), we evaluate the mean value of the dissipation rate in deep clouds to be $\sim$600 cm^2 s^{-3}, which is about 6 times higher than in small cumulus clouds. The factors for drop–drop and graupel–drop collision kernels used in the calculations are presented in Tables 1 and 2, respectively. Zero factors in Table 2 are not related to turbulence effects, but rather reflect the fact that corresponding particles do not collide.

Note that the factors presented in the tables are referred to as just a preliminary or an expert estimation. We do not claim that the factors provide precise parameterization of turbulent effects on drop–drop and drop–graupel collisions.

h. Collisional breakup

A new procedure of collisional breakup has recently been implemented into the HUCM to describe the instability and fragmentation of large raindrops. This scheme is based on the parameterization of Low and List (1982) as well as Beard and Ochs (1995). Using the Beard and Ochs (1995) parameterization is essential to parameterize the coalescence efficiency of small raindrops. The numerical method by Bleck (1970) is applied to break up terms of the stochastic equation. A more detailed documentation of the breakup scheme, its sensitivities, and a comparison of modeled and observed

TABLE 1. Factors indicating an increase in the drop–drop collision kernels due to the turbulence/inertia mechanism.

Drop radius, μm																			
	2	2.5	3.2	4	5	6.4	8	10	13	16	20	25	32	40	51	64	81	102	128
Drop radius, μm																			
2	3.3	3.3	3.3	3.3	3.3	3.3	3.3	3.3	3.1	2.7	2.3	2.1	1.8	1.6	1.3	1.3	1.3	1.3	1.3
2.5	3.3	3.3	3.3	3.3	3.3	3.3	3.3	3.3	3.1	2.7	2.3	2.1	1.8	1.6	1.3	1.3	1.3	1.3	1.3
3.2	3.3	3.3	3.3	3.3	3.3	3.3	3.3	3.3	3.1	2.7	2.3	2.1	1.8	1.6	1.3	1.3	1.3	1.3	1.3
4	3.3	3.3	3.3	3.3	3.3	3.3	3.3	3.3	3.1	2.7	2.3	2.1	1.8	1.6	1.3	1.3	1.3	1.3	1.3
5	3.3	3.3	3.3	3.3	3.3	3.3	3.3	3.3	3.1	2.7	2.3	2.1	1.8	1.6	1.3	1.3	1.3	1.3	1.3
6.4	3.3	3.3	3.3	3.3	3.3	3.3	3.3	3.3	3.1	2.7	2.3	2.1	1.8	1.6	1.3	1.3	1.3	1.3	1.3
8	3.3	3.3	3.3	3.3	3.3	3.3	3.3	3.3	3.1	2.7	2.3	2.1	1.8	1.6	1.3	1.3	1.3	1.3	1.3
10	3.3	3.3	3.3	3.3	3.3	3.3	3.3	3.3	3.1	2.7	2.3	2.1	1.8	1.6	1.3	1.3	1.3	1.3	1.3
13	3.1	3.1	3.1	3.1	3.1	3.1	3.1	3.1	2.9	2.6	2.3	2.1	1.8	1.6	1.3	1.3	1.3	1.3	1.3
16	2.7	2.7	2.7	2.7	2.7	2.7	2.7	2.7	2.6	2.4	2.2	2	1.8	1.5	1.3	1.3	1.3	1.3	1.3
20	2.3	2.3	2.3	2.3	2.3	2.3	2.3	2.3	2.3	2.2	2.1	2	1.7	1.4	1.3	1.3	1.3	1.3	1.3
25	2.1	2.1	2.1	2.1	2.1	2.1	2.1	2.1	2.1	2	2	1.9	1.7	1.4	1.3	1.3	1.3	1.3	1.3
32	1.8	1.8	1.8	1.8	1.8	1.8	1.8	1.8	1.8	1.8	1.7	1.7	1.5	1.4	1.3	1.3	1.3	1.3	1.3
40	1.6	1.6	1.6	1.6	1.6	1.6	1.6	1.6	1.6	1.5	1.4	1.4	1.4	1.4	1.3	1.3	1.3	1.3	1.3
51	1.3	1.3	1.3	1.3	1.3	1.3	1.3	1.3	1.3	1.3	1.3	1.3	1.3	1.3	1.3	1.3	1.3	1.3	1.3
64	1.3	1.3	1.3	1.3	1.3	1.3	1.3	1.3	1.3	1.3	1.3	1.3	1.3	1.3	1.3	1.3	1.3	1.3	1.3
81	1.3	1.3	1.3	1.3	1.3	1.3	1.3	1.3	1.3	1.3	1.3	1.3	1.3	1.3	1.3	1.3	1.3	1.3	1.3
102	1.3	1.3	1.3	1.3	1.3	1.3	1.3	1.3	1.3	1.3	1.3	1.3	1.3	1.3	1.3	1.3	1.3	1.3	1.3
128	1.3	1.3	1.3	1.3	1.3	1.3	1.3	1.3	1.3	1.3	1.3	1.3	1.3	1.3	1.3	1.3	1.3	1.3	1.3

TABLE 2. Factors indicating an increase in the graupel–drop collision kernels due to the turbulence/inertia mechanism.

| Graupel bulk radius, μm	Drop radius, μm																							
	2	2.5	3.2	4	5	6.4	8	10	13	16	20	25	32	40	51	64	81	102	128	161	203	256	323	406
2.7	0	0	0	0	0	0	0	1	1.1	1.2	1.3	1.3	1.3	1.3	1.3	1.3	1.3	1	1	1	1	1	1	1
3.4	0	0	0	0	0	0	0	1	1.2	1.2	1.3	1.3	1.3	1.3	1.3	1.3	1.3	1	1	1	1	1	1	1
4.3	0	0	0	0	0	0	0	1	1.2	1.3	1.3	1.3	1.4	1.4	1.4	1.4	1.3	1	1	1	1	1	1	1
5.4	0	0	0	0	0	0	0	1	1.2	1.3	1.3	1.4	1.5	1.4	1.4	1.4	1.3	1	1	1	1	1	1	1
6.9	0	0	0	0	0	0	0	1	1.3	1.3	1.4	1.5	1.5	1.5	1.5	1.5	1.4	1	1	1	1	1	1	1
8.6	0	0	0	0	0	0	0	1	1.3	1.3	1.5	1.5	1.5	1.5	1.5	1.5	1.4	1	1	1	1	1	1	1
11	0	0	0	0	0	0	0	1	1.3	1.4	1.5	1.6	1.6	1.6	1.6	1.5	1.5	1	1	1	1	1	1	1
14	0	0	0	0	0	0	0	1	1.3	1.5	1.6	1.7	1.7	1.7	1.7	1.6	1.5	1	1	1	1	1	1	1
17	0	0	0	0	0	0	0	1	1.4	1.5	1.7	1.8	1.9	1.8	1.7	1.7	1.5	1	1	1	1	1	1	1
22	0	0	0	0	0	0	0	1	1.5	1.6	1.8	1.9	2	1.9	1.8	1.7	1	1	1	1	1	1	1	1
27	0	0	0	0	0	0	0	1	1.6	1.7	2	2.1	2.2	2.1	2.1	1.9	1.7	1	1	1	1	1	1	1
35	0	0	0	0	0	0	0	1	1.9	2	2.3	2.4	2.5	2.4	2.3	2.1	1.7	1	1	1	1	1	1	1
43	0	0	0	0	0	0	0	1	2.4	2.5	2.7	2.7	2.8	2.7	2.7	2.3	1.7	1.1	1.1	1.1	1	1	1	1
55	0	0	0	0	0	0	0	1	3.1	3.1	3.2	3.2	3.2	3.1	3.1	2.6	1.7	1.1	1.1	1.1	1	1	1	1
69	0	0	0	0	0	0	0	1.1	3.3	3.3	3.5	3.5	3.4	3.3	3.3	2.7	1.7	1.2	1.1	1.1	1	1	1	1
87	0	0	0	0	0	0	0	1.1	3.3	3.3	3.5	3.5	3.4	3.3	3.3	2.7	1.7	1.2	1.1	1.1	1	1	1	1
109	0	0	0	0	0	0	1.1	1.1	3.3	3.3	3.3	3.3	3.3	3.3	3.3	2.7	1.7	1.3	1.2	1.1	1	1	1	1
137	0	0	0	0	0	1.1	1.1	1.1	3.1	3.1	3.1	3.1	3.1	3.1	3.1	2.8	1.8	1.3	1.2	1.1	1	1	1	1
174	0	0	0	0	0	1.1	1.1	1.1	2.7	2.7	2.8	2.8	2.9	3	3	2.8	1.9	1.3	1.2	1.1	1	1	1	1
219	0	0	0	0	1.1	1.1	1.1	1.1	2.5	2.5	2.5	2.5	2.6	2.8	2.8	2.7	2	1.3	1.2	1.1	1	1	1	1
276	0	0	0	1.1	1.1	1.1	1.1	1.1	2.3	2.3	2.3	2.3	2.4	2.5	2.5	2.3	2	1.2	1.2	1.1	1.1	1	1	1
348	0	0	1.1	1.1	1.1	1.1	1.1	1.1	2.1	2.1	2.1	2.2	2.2	2.3	2.3	2.2	1.9	1.2	1.1	1.1	1.1	1	1	1
438	0	1.1	1.1	1.1	1.1	1.1	1.1	1.1	1.9	1.9	2	2	2.1	2.1	2.1	2.1	1.8	1.2	1.1	1.1	1.1	1	1	1
552	1.1	1.1	1.1	1.1	1.1	1.1	1.1	1.1	2	1.9	1.9	1.9	1.9	1.9	1.9	2	1.9	1.1	1.1	1.1	1.1	1	1	1
695	1.1	1.1	1.1	1.1	1.1	1.1	1.1	1.1	1.7	1.7	1.7	1.7	1.7	1.8	1.8	1.9	1.9	1.1	1.1	1.1	1.1	1	1	1
876	1.1	1.1	1.1	1.1	1.1	1.1	1.1	1.1	1.6	1.6	1.6	1.6	1.5	1.6	1.6	1.7	1.6	1.2	1.1	1.1	1.1	1	1	1
1103	1.1	1.1	1.1	1.1	1.1	1.1	1.1	1.1	1.5	1.5	1.5	1.6	1.7	1.7	1.7	1.7	1.7	1.2	1.1	1.1	1	1	1	1
1390	1.1	1.1	1.1	1.1	1.1	1.1	1.1	1.1	1.4	1.5	1.5	1.5	1.6	1.6	1.7	1.7	1.7	1.2	1.1	1.1	1	1	1	1
1751	1.1	1.1	1.1	1.1	1.1	1.1	1.1	1.1	1.3	1.3	1.5	1.5	1.5	1.5	1.5	1.5	1.5	1.2	1.1	1.1	1	1	1	1
2206	1.1	1.1	1.1	1.1	1.1	1.1	1.1	1.1	1.2	1.3	1.3	1.4	1.4	1.4	1.5	1.5	1.4	1.1	1.1	1.1	1	1	1	1
2780	1.1	1.1	1.1	1.1	1.1	1.1	1.1	1.1	1.1	1.2	1.3	1.3	1.3	1.3	1.3	1.3	1.3	1.1	1.1	1.1	1	1	1	1
3502	1.1	1.1	1.1	1.1	1.1	1.1	1.1	1.1	1.1	1.2	1.2	1.2	1.3	1.3	1.3	1.3	1.3	1.1	1.1	1.1	1	1	1	1
4412	1.1	1.1	1.1	1.1	1.1	1.1	1.1	1.1	1.1	1.2	1.2	1.2	1.3	1.3	1.3	1.3	1.3	1.1	1.1	1.1	1	1	1	1
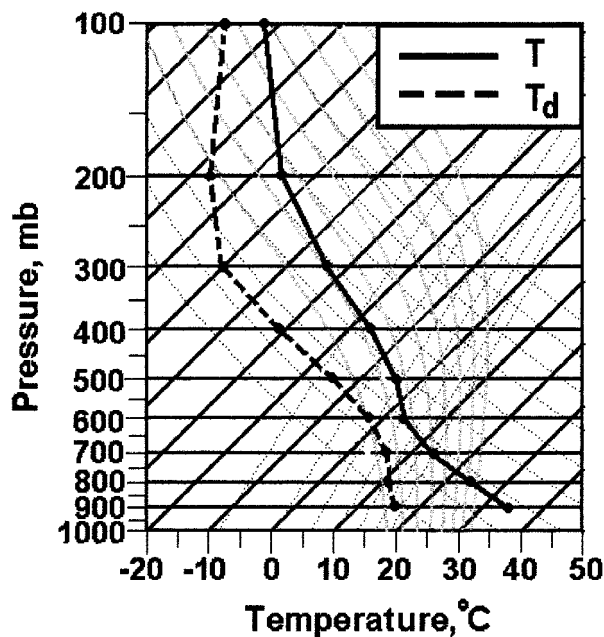
FIG. 4. The Midland, Texas, sounding data of 13 Aug 1999.

raindrop size distributions is given by Seifert et al. (2005).

3. Simulation of a narrow droplet size distribution in growing continental clouds

a. Data and conditions of the simulations

One of the most difficult problems in the Eulerian spectral bin models is the artificial spectrum broadening at the diffusion stage of droplet growth. The latter prevents the reproduction of narrow droplet spectra formed in continental clouds growing in smoky air. To verify the ability of the new version of HUCM to reproduce such spectra, we used as an example for the simulations Texas clouds observed by Rosenfeld and Woodley (2000) on 13 August 1999. The corresponding Midland, Texas, sounding data are shown in Fig. 4. The cloud base and freezing levels are located at about 3.2 km (10°C) and 4.5 km, respectively. According to the sounding, the wind velocity increases from 4 m s^{-1} near the surface to about 7 m s^{-1} at the level of 400 hPa, remaining unchanged aloft. Surface temperature was assumed to be time independent during the period of cloud

evolution. To calculate the initial CCN size distribution, Eq. (2) was used with $N_o = 1260$ cm^{-3} and $k = 0.308$. The cutoff CCN size was taken equal to 0.6 μm (the corresponding radius of activated droplets is about 2.5 μm).

Simulations of a deep Texas cumulus cloud were carried out using the HUCM option, in which aerosol particle concentration is assumed to be height independent. The size of the computational area is 64 km $\times$ 16 km. The development of a convective cloud was triggered by a 10-min duration temperature heating in the boundary layer within the region of 5 km $\times$ 2 km in the horizontal and in the vertical direction, respectively. At time of the cloud formation, the vertical velocity at the cloud base was about 2.5 m s^{-1}.

Two numerical experiments are referred to as controls. In the first one, the turbulent/inertia effects were not taken into account; in the second one, the turbulent/inertia effects were included. The purpose of the sensitivity experiments discussed below is to indicate some numerically related mechanisms that hinder the reproduction of narrow spectra in SBM models.

b. The choice of the model resolution

Clark (1974a,b) found a significant broadening of the droplet spectra with the decreasing resolution of a vertical cloud column, where the vertical airmass flux was assumed to be constant. In multidimensional models, the vertical velocity depends on the model resolution. Since the vertical velocity (especially at the cloud base) substantially influences the dynamics and microphysics of simulated clouds, the utilization of the improper resolution is another source of errors in the reproduction of the droplet spectrum evolution. To test the sensitivity of the results to the grid resolution in the horizontal direction, three experiments (turbulent effects are included) with horizontal resolutions of 1 km, 500 m, and 250 m have been performed. The fields of the vertical velocities in these experiments at 30 min are shown in Figs. 5a–c. The vertical velocity maximum in the case of the 1-km resolution (11 m s^{-1}) turns out to be significantly lower than the maxima in two other experiments ranging from 21.5 m s^{-1} (500-m resolution) to 25.5 m s^{-1} (250-m resolution). The vertical velocity fields, as well as all other fields in the experiments with 500- and 250-m resolutions, are rather similar and differ significantly from those in the experiment with the 1-km resolution. We attribute this result to the fact that the simulated deep convective cloud is a few kilometers in diameter. In this case, the 1-km resolution is not sufficient, as the utilization of such resolution leads to significant errors in microphysical simulations. For instance, in the experiment with the 1-km horizontal grid resolution, the lower velocity results in about a 30%– 40% lower droplet concentration. As a result, in the experiment with the 1-km horizontal grid resolution, raindrops are formed faster and a few kilometers lower
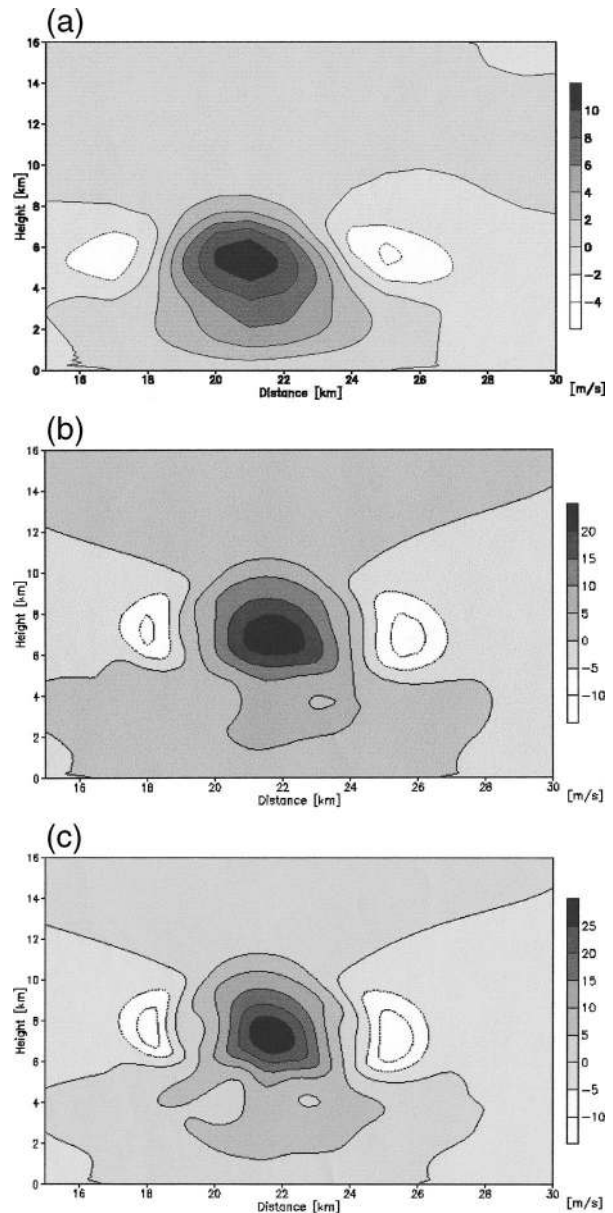

FIG. 5. Vertical velocity fields at 30 min in experiments with the horizontal resolution of (a) 1 km, (b) 500 m, and (c) 250 m.

than in the experiments with higher horizontal model resolutions. All this leads to significant differences in ice microphysics as well.

To test the sensitivity of the results to the vertical model resolution, supplemental simulations have been performed with vertical grid increments of 60, 125, 250, and 400 m. To resolve comparatively narrow zones in clouds playing an important role in cloud evolution, the vertical resolution must be high enough. For instance, a significant fraction of droplets is nucleated within a narrow layer above the cloud base, and the Hallet–Mossop splintering mechanism is active within a comparatively narrow range of temperatures from $-3°$ to $-8°$C,
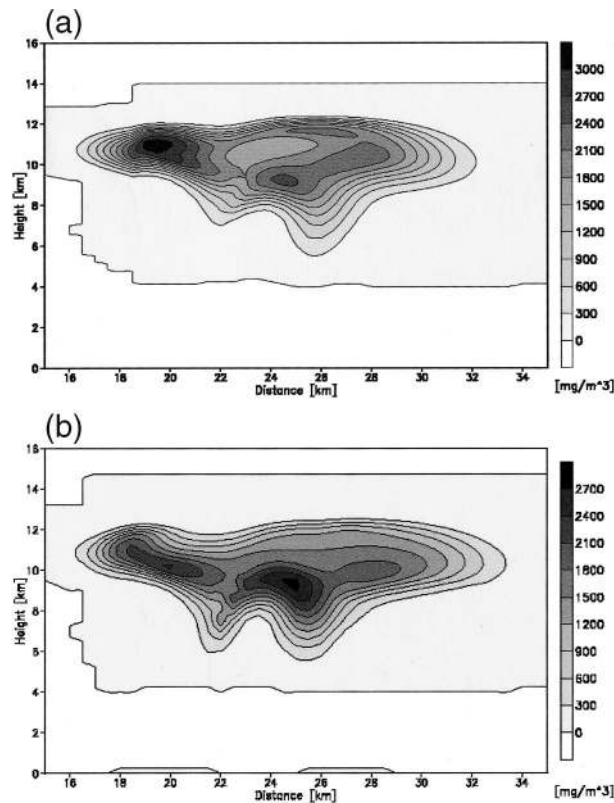
FIG. 6. Fields of graupel content in experiments with vertical resolution of the model grid of (a) 125 m and (b) 250 m at 40 min.

the zone of effective collisions, as well as that of efficient riming, can be also rather narrow in the vertical direction.

Contents and concentrations of different hydrometeors in the experiment with the 400-m vertical grid resolution differ significantly from those in other experiments. At the same time, the difference in the results between the experiments with 60- and 125-m vertical grid increments is much less than that in experiments with 250- and 125-m increments. As an example, we present Figs. 6a–b, which show graupel contents at 40 min in experiments with 125- and 250-m grid increments, respectively. The general structures of the fields, as well as the maximum values, are in fact similar. However, the field calculated with a 125-m increment reproduces more details; for instance, one can see the area of small graupel content in the zone of high vertical velocity at $x = 23$ km and $z = 11$ km.

Proceeding from the results of these experiments, we chose the spatial steps to be 250 m in the horizontal direction and 125 m in the vertical direction for the simulation of deep cumulus clouds. Simulation of smaller cumulus clouds would require an even higher horizontal resolution; for instance, Ovtchinnikov et al. (2000) used a 100-m resolution for the simulation of cumulus clouds with a top height of a few kilometers.

c. Factors leading to artificial spectrum broadening

In this section, we will discuss problems arising in the process of simulating narrow droplet size distributions in continental-type clouds using the Eulerian cloud models. As it is known, in studies dedicated to precise simulations of droplet spectra using Lagrangian parcel models, special attention is paid to the problem of preventing artificial droplet spectrum broadening (Cooper et al. 1997; Pinsky and Khain 2002). The diffusion growth of droplets in such models is often calculated on a variable mass grid, without remapping size distributions on a regular mass grid.

The problem of reproducing a narrow droplet spectrum becomes more complicated in the Eulerian cloud models, because the size distributions obtained by diffusional drop growth should be remapped into a regular mass grid at each time step (see discussions in Liu et al. 1995; Bott 1998; Khain et al. 2000). To illustrate possible sources of the numerical droplet spectrum broadening, the droplet mass spectra formed in the control experiments are compared with those formed in two sensitivity experiments (SE1 and SE2). Experiment SE1 was performed to illustrate the numerical broadening induced by the utilization of the original Kovetz and Olund (1969) procedure (used, e.g., by Takahashi 1976; Khain and Sednev 1996; Geresdi 1998) at each microphysical time step $\Delta t_{\text{diff},n}$, that is, much more frequently than in the control runs. Experiment SE2 was carried out to show the effect of "turbulent mixing" terms additionally included in the equations for size distribution functions.

Figure 7a shows the droplet mass distributions along the cloud axis at $t = 30$ min in the control run with no turbulent effects on collisions included. One can see that the droplet spectrum remains narrow up to the 9-km level. The maximum of the drop mass distribution is centered at 10 μm at 9 km, which is in reasonable agreement with the observations of Rosenfeld and Woodley (2000), indicating the mean volume radius of 8.5 μm at this height. Figure 7b illustrates the mass droplet spectra at 30 min in experiment SE1. One can see that more frequent utilization of the mass remapping procedure leads to a significant acceleration of raindrop formation compared to the control run.

It is common practice with Eulerian cloud models to include turbulent viscosity terms in the equations for size distribution functions (e.g., Khain and Sednev 1996; Kogan 1991). Figure 7c illustrates the mass droplet spectra at 30 min in experiment SE2 similar to the control one, except for viscosity terms additionally included into the equations for size distribution functions. The comparison of the spectra plotted in Figs. 7a and 7c shows that the mixing of droplet size spectra between levels separated in the vertical direction by 125 m leads to the artificial occurrence of smaller droplets at higher levels and to larger droplets near the cloud base. In cases where the vertical resolution is a
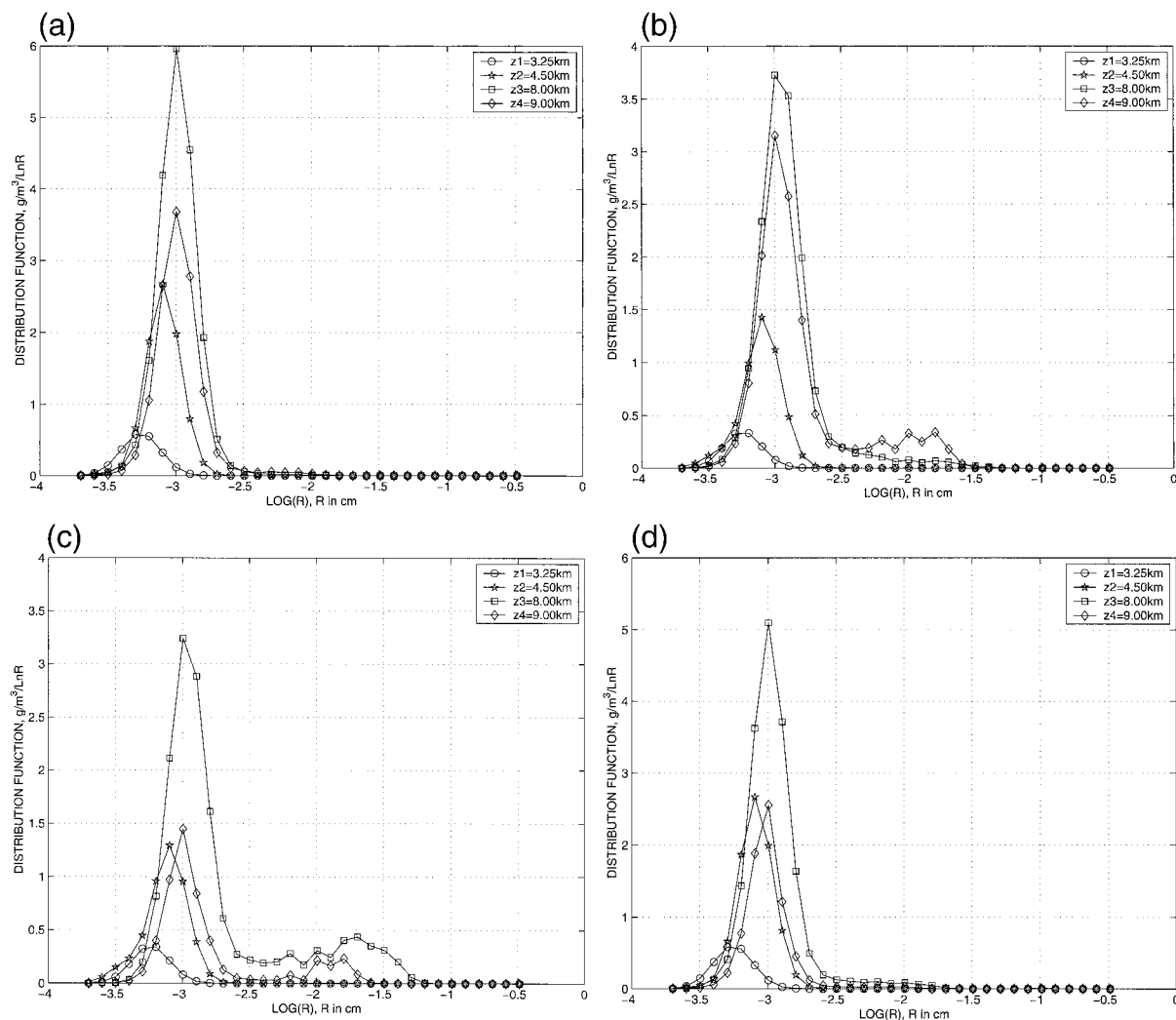
FIG. 7. (a) Droplet mass distributions at different heights along the cloud axis at $t = 30$ min in the control experiment. One can see that the droplet spectrum remains narrow up to the level of 9 km. (b) Same as in (a), but in a supplemental experiment with a more frequent utilization of the mass remapping procedure. (c) The same as in (b), but in a supplemental experiment in which the turbulent mixing (viscosity) terms are additionally included into the equations for size distribution functions. (d) Droplet mass distributions at different heights along the cloud axis at 30 min in the control experiment when turbulence/inertia effects on collisions are included.

few hundred meters (resolution typical of the majority of cloud models), the artificial broadening should be more pronounced.

Note that mixing as it is represented by the k theory is applied for conservative quantities, which do not change at the distances of the mixing length (several tens of meters). Such a procedure leads to the spatial homogenization of the mixed variable. The assumption that the size distribution is a conservative quantity can be used only at very small distances, at which one can assume that essentially no droplet growth occurs during the mixing of parcels (Clark 1976). At higher distances, the drop size distribution cannot be considered as a conservative quantity; it changes significantly during diffusional growth at distances of several tens of meters. In this case, more complicated expressions should be

used for the description of the mixing (Clark 1976). The application of the standard mixing (k theory) to the size distributions in case of significant separation distances between the neighboring model levels leads to the above-mentioned spectrum broadening. We suppose that the increase in the droplet spectrum broadening with a decrease in the resolution found by Clark (1974a,b) is related to the effect discussed above. Clark found that the increase in the resolution in the Eulerian approach led to a better agreement with the prediction of the Lagrangian model, in which no vertical mixing of size distributions was taken into account.

Note that the effects of turbulent viscosity terms are significant in the case of simulating deep continental clouds with a very narrow droplet spectrum. In maritime clouds, the droplet spectra are wide, and the artificial

broadening introduced numerically does not, supposedly, play such a significant role.

Yet another factor leading to the formation of the wider droplet spectrum is a crude model resolution in the horizontal direction. As was mentioned above, a decrease in the resolution leads to a decrease in the vertical velocity and, consequently, to a decrease in supersaturation and in the droplet concentration. Thus, the utilization of the crude resolution turns model clouds into more "maritime" ones.

Along with the artificial mechanisms of the droplet spectrum broadening discussed above, there is a physically based turbulence/inertia mechanism leading to the acceleration of particle collisions in turbulent clouds. Figure 7d shows the droplet mass distributions at different heights along the cloud axis at $t = 30$ min in the control experiment, with turbulence/inertia effects on collisions included. The comparison with the spectra plotted in Fig. 7a shows that turbulence leads to the droplet spectrum broadening and the formation of small raindrops (with radii over 100 μm) at high levels. However, the concentration of large drops is small, so that the spectrum remains narrow up to the level of homogeneous freezing. As can be seen from the comparison with Figs. 7b–c, the droplet spectrum broadening, induced by turbulence/inertia effects, turns out to be less pronounced when compared with the numerically induced broadening. In case the artificial spectrum broadening in a certain cloud model occurs, the implementation of turbulence/inertia effects on collisions would lead to an additional, undesirable (in this case) acceleration of precipitation formation.

4. Applications of the model to the simulation of cloud microphysics and investigations of aerosol effects

a. Design of experiments

In this section we present some examples illustrating the effects of new processes (collision breakup, melting, and aerosol distributions) on cloud microphysics and precipitation.

To illustrate aerosol effects on deep continental clouds, we will discuss the results of numerical experiments, in which aerosol particles with characteristics of maritime aerosol were used in the Texas sounding. The maritime aerosol distribution was characterized by parameters $N_o = 100$ cm^{-3} and $k = 0.462$ in Eq. (2). In addition, in accordance with the measurements by Hudson (1993), it was assumed that there were no small CCN that could be activated at supersaturations exceeding 1.0%. Experiments with continental (C) and maritime (M) aerosols will be referred to as C- and M-Texas simulations, respectively.

To illustrate aerosol effects on deep convective clouds arising under maritime thermodynamic conditions, we simulated clouds using profiles from the 1200 UTC
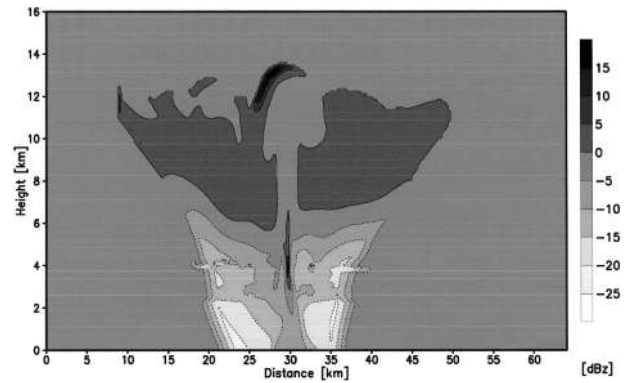

FIG. 8. The difference in the radar reflectivity fields produced by clouds simulated by using the Texas temperature profiles and maritime aerosols with and without breakup included.

sounding on board the Canadian ship *Quadra,* on day 261 of the Global Atmospheric Research Programme (GARP) Atlantic Tropical Experiment (GATE) experiments. This sounding has been used in many previous modeling studies of maritime convection (e.g., Turpeinen and Yau 1981; Ferrier and Houze 1989). Two AP distributions (M and C) described above were used in the simulations with the GATE profiles as well. Corresponding simulations will be referred to as M- and C-GATE simulations.

b. Effects of breakup on the microstructure of clouds and precipitation

Since a new procedure of collisional breakup has been implemented recently into the HUCM, it is of interest to investigate its effect on rain formation and accumulated rain amount. Figure 8 shows the difference in the radar reflectivity fields for the M-Texas simulations with and without breakup at $t = 1$ h. The radar reflectivity was calculated according to its definition (using the size distributions) as described by Khain and Sednev (1996). One can see that radar reflectivity with breakup is lower near the surface, indicating the lower amount of large raindrops. At the same time higher reflectivity above the freezing level (4.2 km) is the result of the formation of additional graupel; raindrops of a smaller size and higher concentration (formed due to the breakup) are advected upward and freeze to graupel. The corresponding fields of graupel content at $t = 1$ h, when the breakup is included (the upper panel), and the difference between the graupel contents in simulations with and without the breakup (the lower panel) are shown in Fig. 9. Similar effects of breakup are found in the simulation with continental aerosols as well.

Analysis of size distribution functions with and without breakup taken into account indicates that breakup changes the shape of size distributions toward the Marshall–Palmer distribution. In a case of strong precipitation under maritime thermodynamic conditions and in
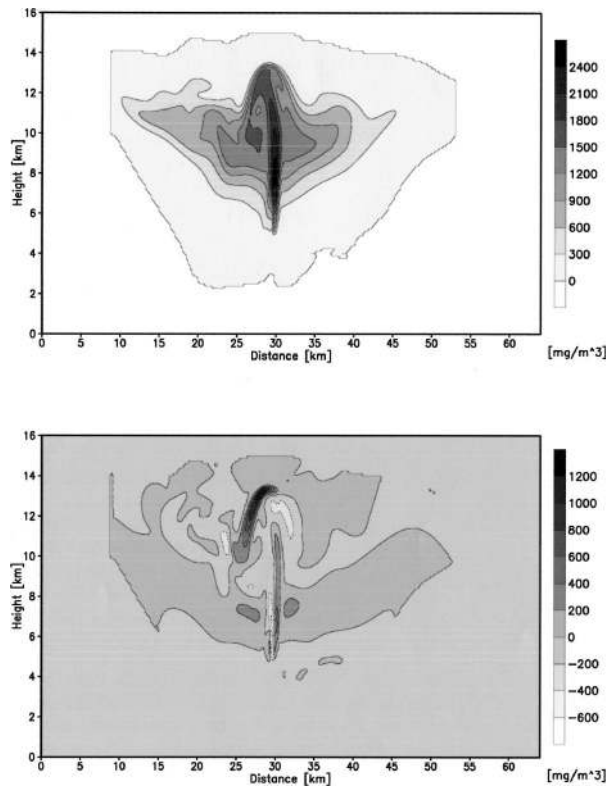
FIG. 9. (a) The graupel content at 3600 s when the breakup is included and (b) the difference between the graupel contents in simulations with and without breakup. The conditions are similar to those of Fig. 8.

maritime aerosols, breakup leads to the formation of raindrop spectra close enough to the equilibrium distribution. The breakup effects on the shape of the raindrop size distributions will be discussed in more detail in a separate paper.

Figures 10a–b show the spatiotemporal dependencies of precipitation rates for the simulations without and with breakup, respectively. One can see that precipitation decreases significantly when the breakup is taken into account. This decrease is especially significant in the zone of maximum precipitation rate. The precipitation decrease and time redistribution are related to the stronger evaporation of precipitating water in simulations when the breakup is taken into account. This effect can be attributed to a larger number of smaller droplets falling through the dry atmosphere, as well as to an increase in the time period during which precipitating particles reach the surface. The spatiotemporal distribution of precipitation in the M-Texas simulation is presented in Figs. 10c–d (without and with breakup, respectively). A significant decrease in precipitation caused by breakup is seen in the case of low aerosol concentration as well. The most significant decrease takes place at $t \approx 40$ min, where intense warm rain takes place. The breakup prevents formation of large raindrops that leads to a ~10–15-min delay in reaching

the precipitation rate maximum and to a shift of the precipitation maximum downwind by ~5 km.

Figure 11 shows the time dependence of the accumulated rain amount in different M- and C-Texas simulations. One can see that the breakup leads to a decrease in the accumulated rain by about 50%. When the breakup is included, the warm rain starts about 10 min later. It can be attributed to the fact that smaller raindrops have lower fall velocities, so that they cannot fall within a strong updraft.

c. Aerosol effects on precipitation and convective heating

In this section we present some examples of aerosol effects on microphysics and thermodynamics of single clouds developed under continental and maritime soundings.

Figure 12 shows fields of rainwater content (RWC) in a continental (Texas) sounding in the continental (left) and maritime (right) aerosol simulations. One can see that in M-aerosol case, RWC is much higher and raindrops reach the surface. At the same time, in the C-case, RWC concentrates around the level of 4–5 km. No precipitation at the surface takes place at this time.

The comparison of spatiotemporal distributions of precipitation in the M-Texas simulation (Figs. 10c–d) with those in the C-Texas simulation (Figs. 10a–b) indicates a crucial increase in precipitation with the decrease in the aerosol concentration. In maritime aerosol, precipitation begins 15–20 min earlier compared with the case of continental aerosol, and reveals a much higher warm-rain amount.

While under the unstable Texas thermodynamic conditions, the cloud depth is limited by the stable stratified layer in the upper troposphere; the cloud depth under the GATE temperature profiles depends on the magnitude and size of temperature fluctuations used for the convection triggering. We simulated single clouds of different top heights by using different widths of the initial temperature fluctuations. The simulations indicate that an increase in the aerosol concentration tends to cause a decrease in precipitation from single convective maritime clouds as well. To produce a similar amount of accumulated rain, a cloud developed in smoky air should be deeper compared to that developed in clean air. Figure 13 shows the fields of the total ice content in C- and M-GATE simulations at 60 min. In the C case, the cloud top reaches ~11 km (determined by the 10-dBZ radar reflectivity level), while in the M case, the cloud-top height was only 8 km. Despite the fact that accumulated rain amounts in both cases are similar, the time dependence of rain accumulation in the maritime and continental aerosols cases are quite different (Fig. 14). In the C case, precipitation starts ~10 min later. In the M case, warm precipitation falls in the course of ~20 min. Later on, the warm precipitation is replaced by the melted rain as seen by the slow rate of rain
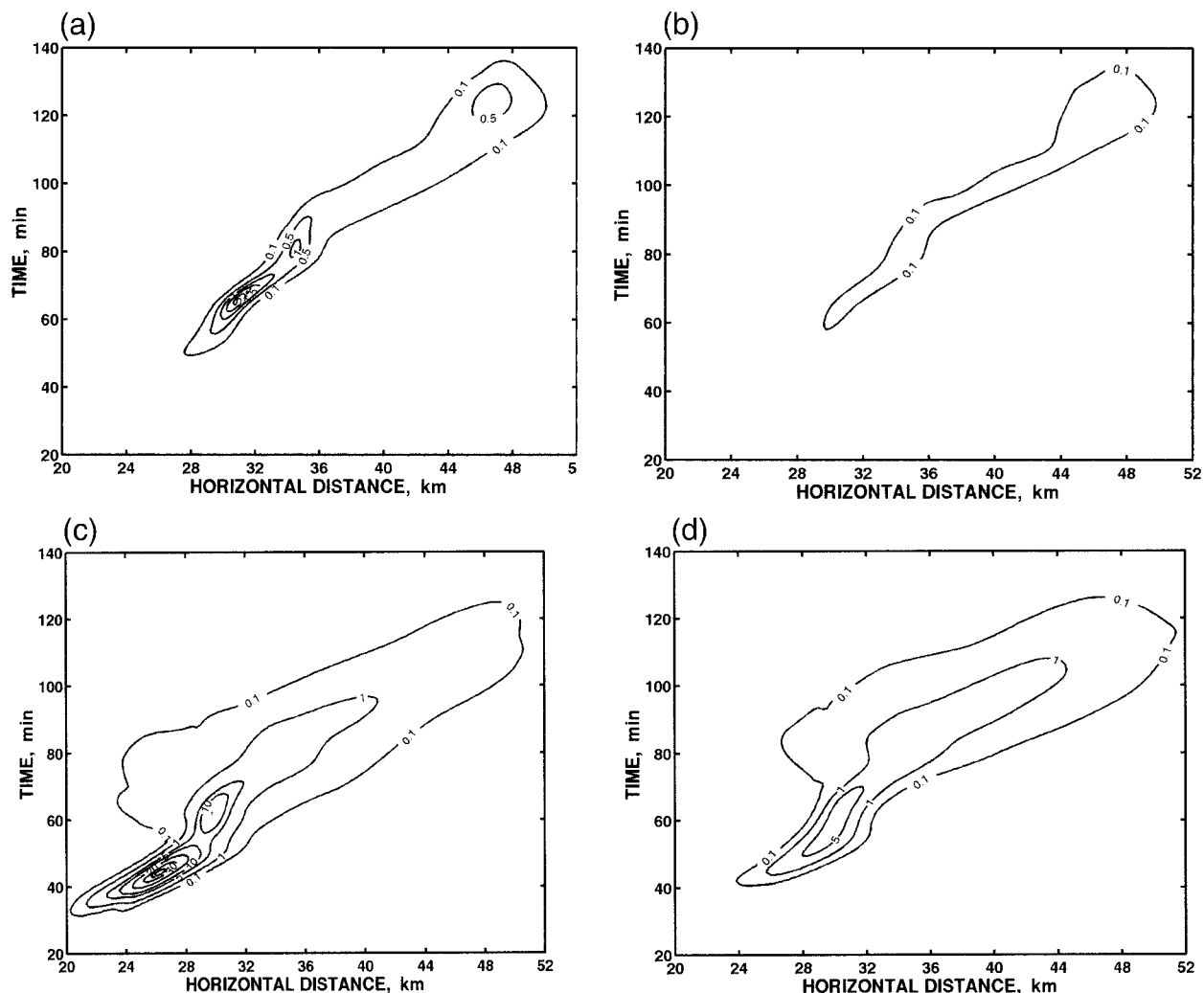
FIG. 10. Spatiotemporal dependencies of precipitation rates for the Texas sounding in simulations (a) without and (b) with the breakup in the continental aerosol case. (c), (d) The same as in (a), (b), but for the maritime aerosol.
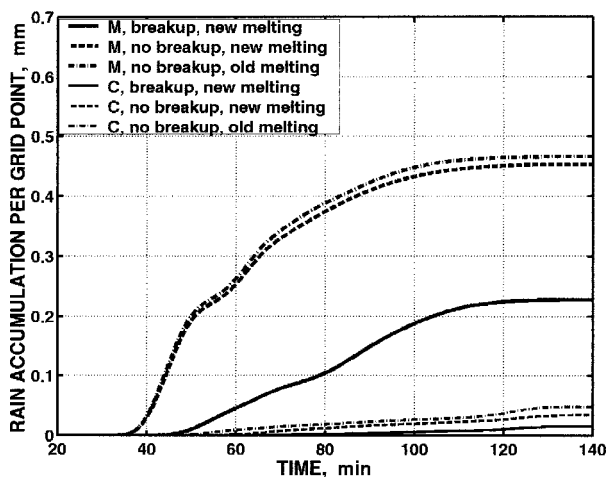

FIG. 11. The time dependence of the accumulated rain in M-Texas and C-Texas experiments with and without the breakup, when new and old immediate melting procedures are included.

accumulation, which terminates in ~90 min. At the same time, in the C case, the contribution of melted rain is much more significant. The cloud lifetime in the continental aerosol case is longer; the precipitation continues even at $t = 120$ min.

The larger precipitation amount from the clouds developed in the maritime aerosol cases compared to the continental aerosol cases means that an increase in the aerosol concentration decreases the net convective heating (caused by the phase transitions in clouds) of the atmosphere. Dependencies of convective heating on the height should be affected by aerosols as well. Clouds developed in the M- and C-GATE cases, which produce a similar accumulated rain, have different depths and, consequently, may have a different vertical distribution of convective heating. The profiles of the convective heating in such clouds are shown in Fig. 15. These profiles were averaged over 2 h of cloud simulation and in the horizontal direction over the whole 64-km com-
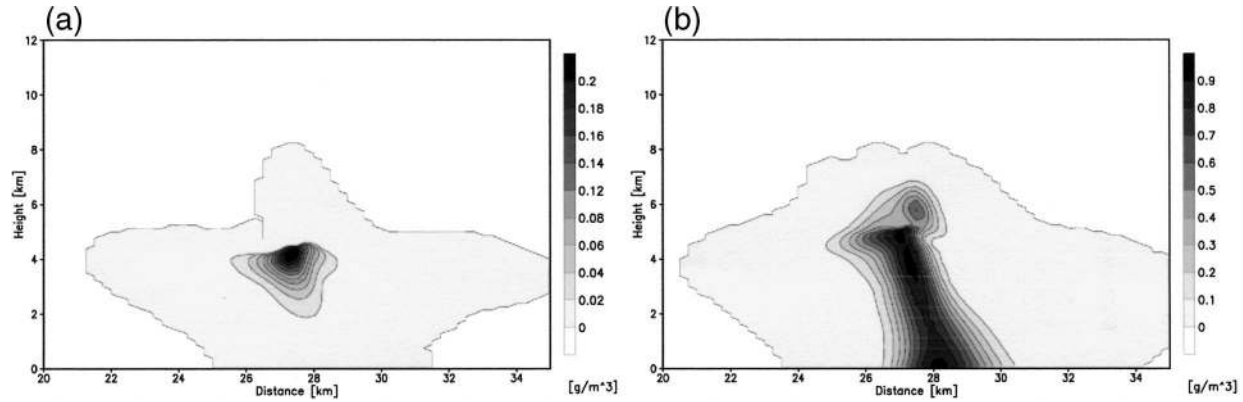
FIG. 12. Fields of RWC in clouds formed in the continental (Texas) sounding in the (a) continental and (b) maritime aerosol simulations (breakup and new melting procedures are included).

putational zone. The dashed and dashed–dotted lines corresponding to positive values of heating indicate the contribution of condensation, deposition, and freezing in the C and M cases, respectively. The dashed and dashed–dotted lines corresponding to the negative heating values represent effects of evaporation, sublimation, and melting. Thick solid and dashed lines indicate the net effect for simulations with continental and maritime aerosols, respectively. The increase in the aerosol concentration leads to a strong increase in heating, both due to the increase in the diffusional growth and the more intense droplet freezing. At the same time, the cooling in the continental aerosol case is much higher because of the higher evaporation of droplets and ice sublimation. The higher droplet evaporation and ice sublimation in the C case can be attributed to the following. In the case of continental aerosol, raindrops and ice particles are, as a rule, smaller than in the case of maritime aerosol, and they reach higher levels. Also, they have the smaller sedimentation velocity. As a result, the time duration of their sedimentation is longer. In addition, being shifted by an environmental wind shear from the zone of cloud updraft, ice particles and drops falling

from higher levels tend to sediment through dry air. At the same time, in the maritime aerosol case, raindrops form at lower levels and fall rapidly down through the cloudy wet air (or in the close vicinity of the clouds), where the air humidity is comparatively high. As a result, the evaporation (and corresponding cooling) in the maritime aerosol case is lower compared to the continental aerosol case. The higher loss in the precipitating mass by the drop evaporation and ice sublimation is the main cause of the lower precipitation efficiency of clouds developed in smoky air. The comparison of the net heating profiles in C- and M-aerosol GATE cases indicates that in the C case, heating is extended to higher levels.

The minimum in the net heating at ~3.5 km in the C-GATE case (Fig. 15) is related to the cooling caused by the melting of ice (mainly graupel). No such minimum is seen in the profile of net convective heating in the M-GATE simulation, indicating a smaller contribution of melted rain in the last case.

The problem of aerosol effects on the convective heating profiles under different conditions will be further elaborated in the next parts of the study.
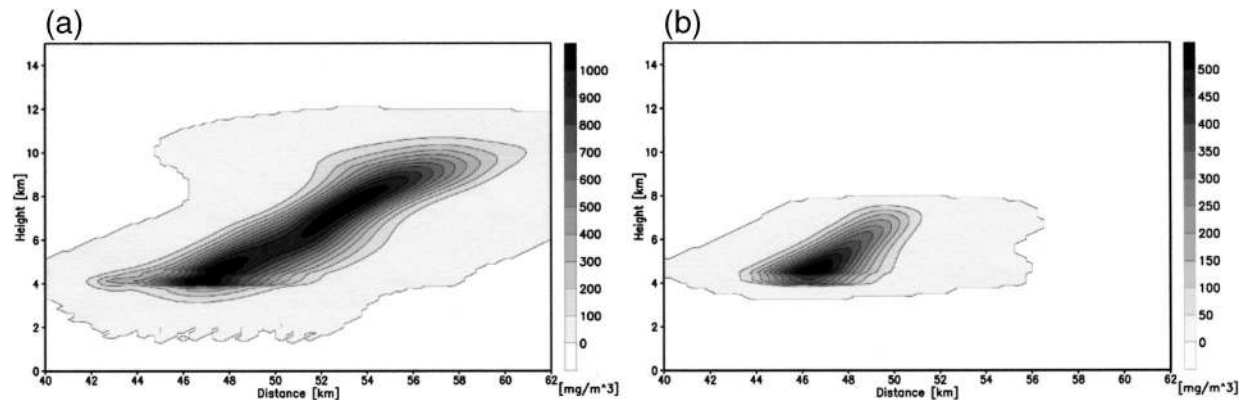

FIG. 13. Fields of ice content in clouds developed in the GATE thermodynamic profiles in the maritime and continental aerosols cases, producing similar accumulated rain amounts.
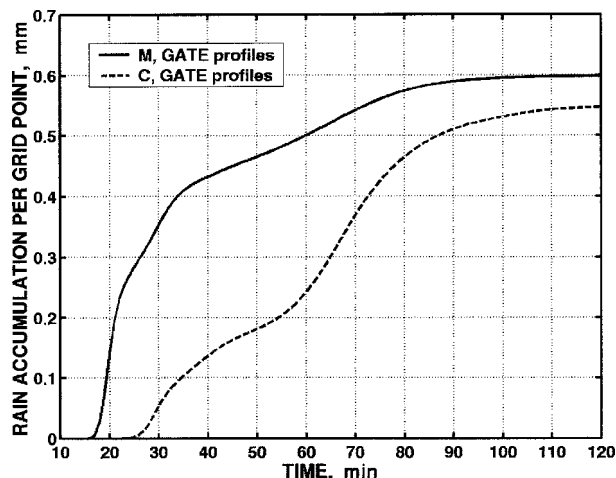
FIG. 14. Time dependence of accumulated rain from single convective clouds developed in the GATE thermodynamic profiles in the maritime and continental aerosol cases.
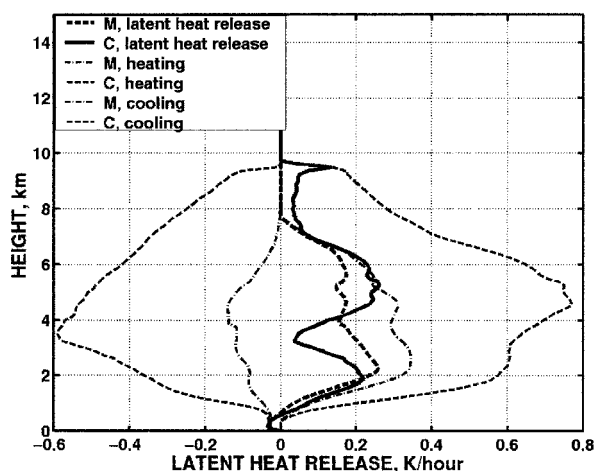
FIG. 15. Vertical profiles of convective heating caused by clouds developed in the GATE temperature profiles in the continental and maritime aerosol cases. The dashed and dashed–dotted lines corresponding to positive values of heating indicate contribution of condensation, deposition, and freezing for continental and maritime aerosol simulations, respectively. The dashed and dashed–dotted lines corresponding to the negative heating values represent effects of evaporation, sublimation, and melting. Thick solid and thick dashed lines indicate the net effect for continental and maritime aerosol simulations, respectively.

d. Microphysical structure of the melting layer

The early version of the HUCM (Khain and Sednev 1996) describes the melting process in a simplified manner; all ice particles penetrating the zone of positive temperatures were assumed to melt immediately. The similar simplification is used in some other models (e.g., Ovtchinnikov et al. 2000). A new melting scheme has been implemented recently. In this scheme, ice particles of different type and size melt at different rates and fall down with different fall velocities, which vary in the course of melting as a result of the change in shape and surface roughness.

We illustrate the microphysical structure of the melting layer when using the results of cloud simulations for the C and M cases under the Texas thermodynamic conditions. Figure 16 shows the fields of the "integral" liquid water fraction in graupel for the continental (left panel) and maritime aerosol (right panel) cases at $t = 85$ min. One can see the significant effect of aerosol on

the structure of the melting layer; graupel in the M-Texas case penetrates the layer with positive temperatures further than in the C case. This can be explained by the fact that in the M case, graupel is larger and settles faster (Fig. 17). At the same time the mass of graupel in the continental aerosol case is higher, as was discussed above. The difference in the graupel content is maximal at 9 km and attains 1.2 g m^{-3} (see Fig. 17c). Figure 18 shows the distribution functions of the liquid water fraction in graupel at different heights below the freezing level (located at 4.2 km) in the continental aerosol case (left) and the maritime aerosol case (right) at $x = 37$ and 36 km, respectively. The corresponding evolution of the graupel mass distribution functions with
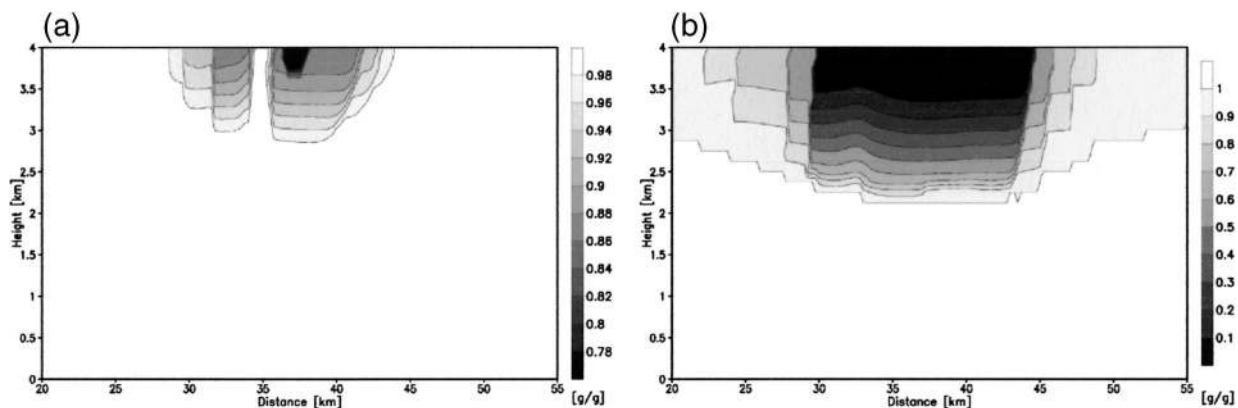

FIG. 16. Fields of the net liquid water fraction in graupel within the melting layer for the (a) continental and (b) maritime aerosols at 5100 s.
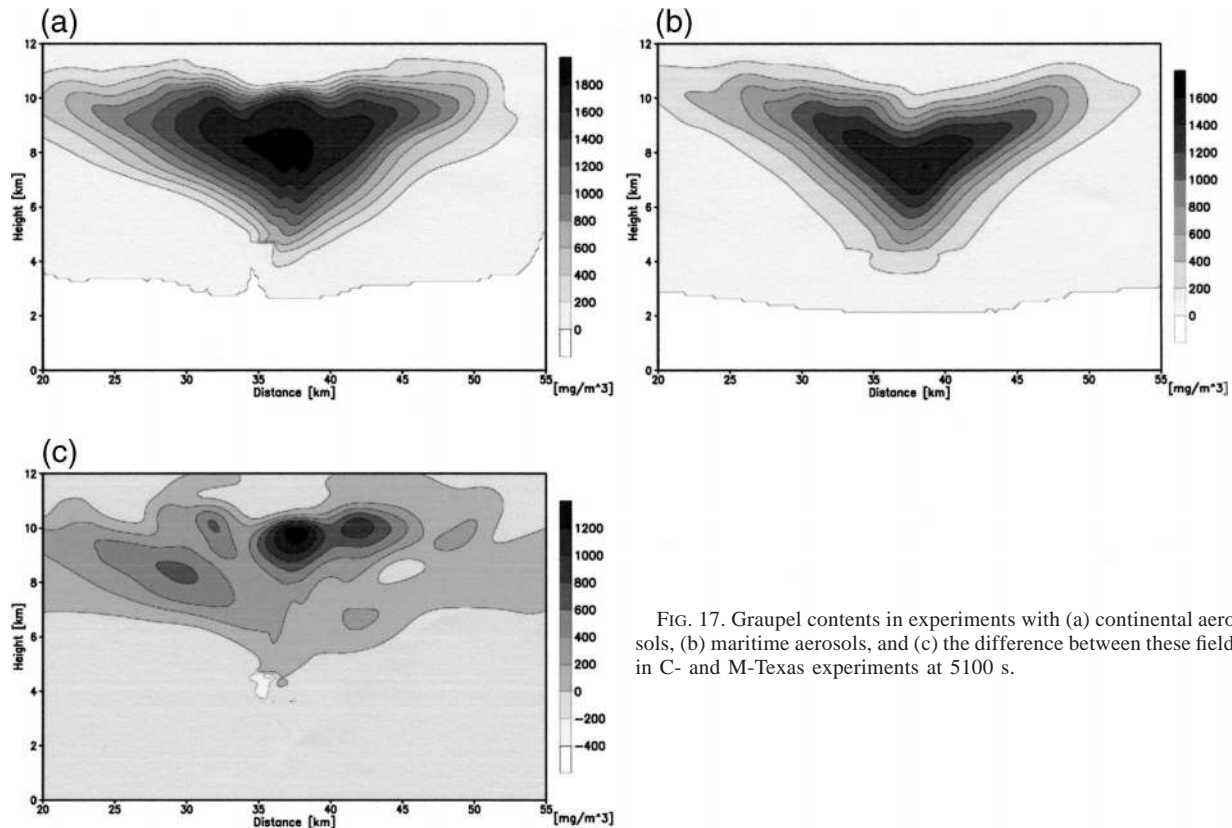
FIG. 17. Graupel contents in experiments with (a) continental aerosols, (b) maritime aerosols, and (c) the difference between these fields in C- and M-Texas experiments at 5100 s.

height during the graupel melting is shown in Fig. 19. One can see in Figs. 18 and 19 that the bins of small masses melt first with a corresponding increase in the liquid fraction from zero to one. The water of completely melted bins is transferred to the corresponding bins in the drop size distribution that can be seen by zero graupel mass distributions for the smallest bins.

Since the size of graupel in the C case is smaller compared to that in the M case, they melt faster within the thinner layer at the time instance.

Similar information is available for snowflakes and hail as well. The detailed information of the microphysical structure of the melting layer is useful for purposes of remote sensing, the identification of stratiform
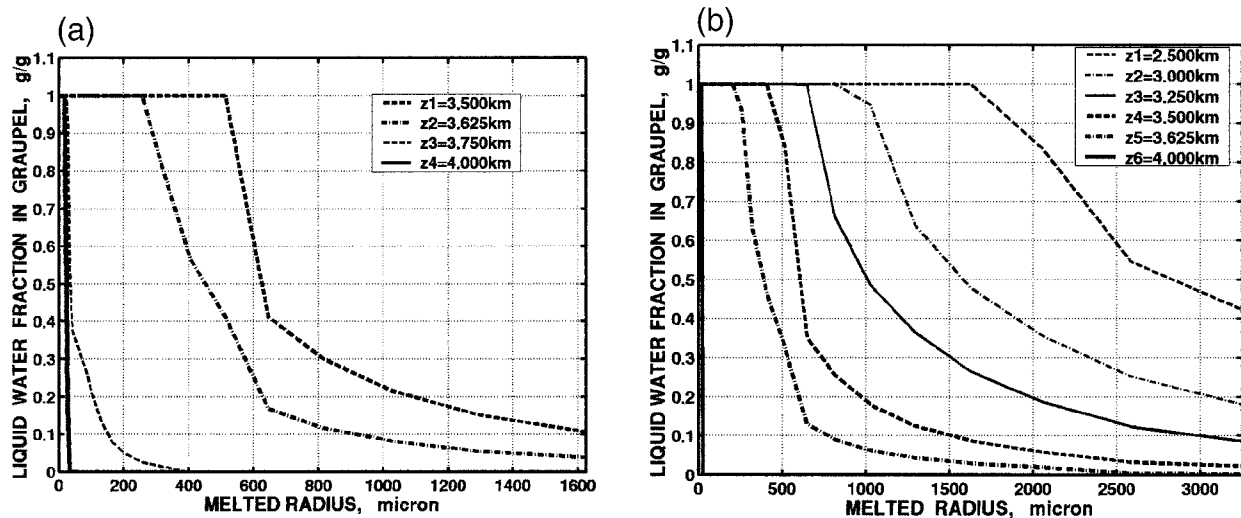

FIG. 18. Distribution functions of the liquid water fraction in melting graupel at different heights below the freezing level in the (a) continental ($x = 37$ km) and (b) maritime aerosol cases ($x = 36$ km) at 5100 s.
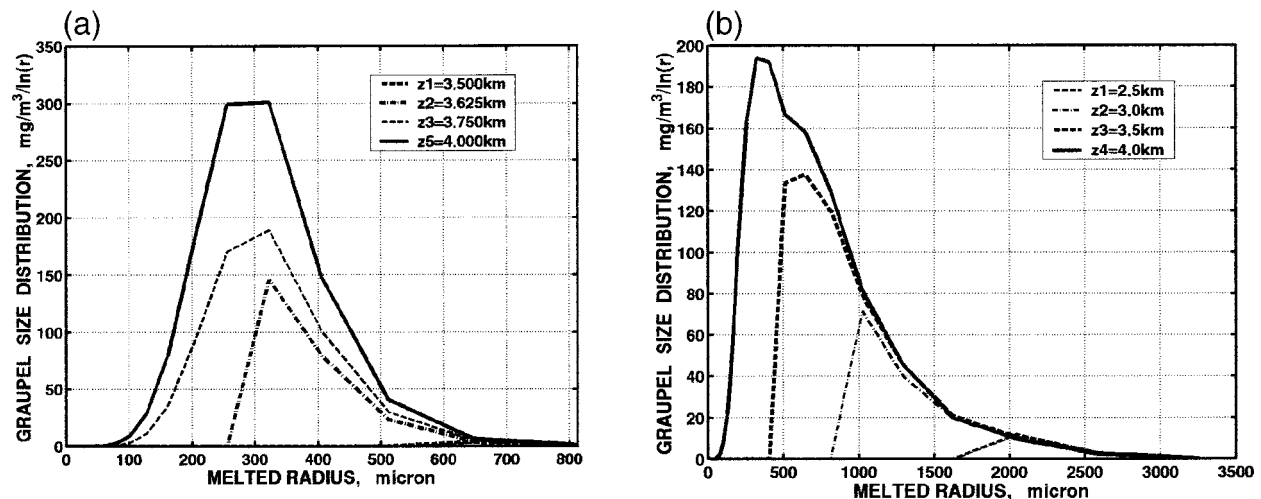
FIG. 19. Graupel mass distribution functions at different heights within the melting layer in cases of the (a) continental ($x = 37$ km) and (b) maritime aerosols ($x = 36$ km) at 5100 s.

clouds from space, etc. As seen in Fig. 11, the detailed melting procedure leads to an insignificant change in precipitation in the simulations performed.

5. Conclusions

The description of the updated Hebrew University Cloud Model (HUCM) is presented. The model is based on the solution of the equation system for size (number) distribution functions for droplets, ice particles of seven types (including three types of ice crystals), and aerosol particles. The presence of the aerosol particles allows the calculation of size distributions of newly nucleated droplets for those both at the cloud base and those entering the cloud through lateral boundaries. The model calculates changes of the CCN concentration and size distribution due to droplet nucleation and advection. The description of drop freezing and primary ice nucleation is based on the semi-Lagrangian approach. The diffusion growth of drops and ice of different shapes is described by means of analytically calculated supersaturations with respect to water and ice. Tables of drop–drop and drop–graupel collision kernels utilized in the model were calculated by using a precise hydrodynamic method suitable for the simulation of drop collisions within a wide range of droplet sizes. The collision efficiencies and kernels are height dependent. The collisional growth was calculated using the efficient Bott's (1998) method, which was extended to ice–water and ice–ice collisions. Turbulence/inertia effects on water–water and ice–water collision rates are taken into account. A novel collisional breakup scheme and a detailed melting scheme developed recently have been implemented into the HUCM.

Three sources of the artificial spectrum broadening in the Eulerian cloud models are discussed: the utilization of the crude spatial resolution, a too-frequent

utilization of the size distribution functions remapping on a regular mass grid, and the utilization of standard k theory to the mixing of the droplet spectra at different levels. A significant reduction of the artificial spectrum broadening in the HUCM made it possible to reproduce a narrow droplet spectrum with parameters similar to those measured in deep Texas summertime clouds even when turbulence/inertia effects were included.

The role of breakup and melting in cloud microphysics is illustrated in several simulations. In the case of a dry continental environment, the breakup leads to a decrease in the precipitation, especially of warm rain. The formation of comparatively small raindrops leads to their ascending in cloud updraft and freezing with the formation of graupel. The magnitude of the effect follows from the Low and List (1982) parameterization, which, probably, overestimates the breakup rate (Axel et al. 2003). Further laboratory and theoretical studies seem to be necessary for a better understanding and parameterization of the breakup phenomena.

The new version of HUCM provides a detailed microphysical structure of the melting layer. The data allow avoiding many assumptions and simplifications about the composition of the water–ice mixture in the melting layer used for the calculation of radiative properties (Bauer et al. 2000). This data can be useful for the development of remote sensing methods, the separation between cumulus and stratiform clouds from satellites, the evaluation of precipitation over large areas, and so on. The data are available upon request.

It is shown that both the precipitation rate and the rain amount depend crucially on the CCN concentration and size distribution. An increase in aerosol (CCN) concentration leads to the formation of smaller droplets and ice particles at higher levels compared to those in the case of maritime aerosols. As a result, the precipitating particles fall down through the dry air layer during a

longer period of time, which leads to a larger precipitation loss in smoky air. Therefore, the clouds developing in the smoky air have lower precipitation efficiency. Different precipitation efficiencies cause different net heating and different vertical distributions of the convective heating in smoky and clean air under similar thermodynamic conditions. Owing to the high sensitivity of different atmospheric phenomena to the convective heating and its vertical distribution, aerosols can affect precipitation and the air circulation at local, mesoscale, and, supposedly, global-scale levels. This problem is the subject of future investigations.

REFERENCES

Andreae, M. O., D. Rosenfeld, P. Artaxo, A. A. Costa, G. P. Frank, K. M. Longo, and M. A. F. Silva-Dias, 2003: Smoking rain clouds over the Amazon. *Science,* **303,** 1337–1342.

Bailey, I. H., and W. C. Macklin, 1968: Heat transfer from artificial hailstones. *Quart. J. Roy. Meteor. Soc.,* **94,** 93–98.

Bauer, P., A. Khain, A. Pokrovsky, R. Meneghini, C. Kummerow, F. Marzano, and J. P. V. Poiares Baptista, 2000: Combined cloud–microwave radiative transfer modeling of stratiform rainfall. *J. Atmos. Sci.,* **57,** 1082–1104.

Beard, K. V., 1976: Terminal velocity and shape of cloud and precipitation drops aloft. *J. Atmos. Sci.,* **33,** 852–864.

——, and H. T. Ochs, 1995: Collisions between small precipitating drops. Part II: Formulas for coalescence, temporary coalescence, and satellites. *J. Atmos. Sci.,* **52,** 3977–3996.

Bleck, R., 1970: A fast approximative method for integrating the stochastic coalescence equation. *J. Geophys. Res.,* **75,** 5165–5171.

Bott, A., 1998: A flux method for the numerical solution of the stochastic collection equation. *J. Atmos. Sci.,* **55,** 2284–2293.

Clark, T. L., 1973: Numerical modeling of the dynamics and microphysics of warm cumulus convection. *J. Atmos. Sci.,* **30,** 857–878.

——, 1974a: A study in cloud phase parameterization using the gamma distribution. *J. Atmos. Sci.,* **31,** 142–155.

——, 1974b: On modelling nucleation and condensation theory in Eulerian spatial domain. *J. Atmos. Sci.,* **31,** 2099–2117.

——, 1976: Use of log-normal distributions for numerical calculations of condensation and collection. *J. Atmos. Sci.,* **33,** 810–822.

Cooper, W. A., R. Bruintjes, and G. K., Mather, 1997: Calculations pertaining to hygroscopic seeding with flares. *J. Appl. Meteor.,* **36,** 1449–1469.

Ferrier, B. S., and R. A. Houze Jr., 1989: One-dimensional time-dependent modeling of GATE cumulonimbus convection. *J. Atmos. Sci.,* **46,** 330–352.

Flossmann, A. I., W. D. Hall, and H. R. Pruppacher, 1985: A theoretical study of the wet removal of atmospheric pollutants. Part I: The redistribution of aerosol particles captured through nucleation and impaction scavenging by growing cloud drops. *J. Atmos. Sci.,* **42,** 583–606.

Geresdi, I., 1998: Idealized simulation of the Colorado hailstorm case: Comparison of bulk and detailed microphysics. *Atmos. Res.,* **45,** 237–252.

Hallett, J., and S. C. Mossop, 1974: Production of secondary ice crystals during the riming process. *Nature,* **249,** 26–28.

Hobbs, P. V., 1993: *Aerosol–Cloud Interaction.* International Geophysics Series, Vol. 54, Academic Press, 237 pp.

Hudson, J. G., 1993: Cloud condensational nuclei near marine cumulus. *J. Geophys. Res.,* **98,** 2693–2702.

Ji, W., and P. K. Wang, 1990: Numerical simulation of three-dimensional unsteady viscous flow past fixed hexagonal ice crystals in the air-preliminary results. *Atmos. Res.,* **25,** 539–557.

Kaufman, Y., and T. Nakajima, 1993: Effect of Amazon smoke on cloud microphysics and albedo—Analysis from satellite imagery. *J. Appl. Meteor.,* **32,** 729–744.

Khain, A. P., and I. Sednev, 1996: Simulation of precipitation formation in the Eastern Mediterranean coastal zone using a spectral microphysics cloud ensemble model. *Atmos. Res.,* **43,** 77–110.

——, D. Rosenfeld, and I. L. Sednev, 1993: Coastal effects in the Eastern Mediterranean as seen from experiments using a cloud ensemble model with a detailed description of warm and ice microphysical processes. *Atmos. Res.,* **30,** 295–319.

——, I. Sednev, and V. Khvorostyanov, 1996: Simulation of coastal circulation in the Eastern Mediterranean using a spectral microphysics cloud ensemble model. *J. Climate,* **9,** 3298–3316.

——, A. Pokrovsky, and I. Sednev, 1999: Some effects of cloud–aerosol interaction on cloud microphysics structure and precipitation formation: Numerical experiments with a spectral microphysics cloud ensemble model. *Atmos. Res.,* **52,** 195–220.

——, M. Ovtchinnikov, M. Pinsky, A. Pokrovsky, and H. Krugliak, 2000: Notes on the state-of-the-art numerical modeling of cloud microphysics. *Atmos. Res.,* **55,** 159–224.

——, M. B. Pinsky, M. Shapiro, and A. Pokrovsky, 2001a: Graupel-drop collision efficiencies. *J. Atmos. Sci.,* **58,** 2571–2595.

——, D. Rosenfeld, and A. Pokrovsky, 2001b: Simulating convective clouds with sustained supercooled liquid water down to −37.5°C using a spectral microphysics model. *Geophys. Res. Lett.,* **28,** 3887–3890.

Khvorostyanov, V. I., A. P. Khain, and E. L. Kogteva, 1989: A two-dimensional non-stationary microphysical model of a three-phase convective cloud and evaluation of the effects of seeding by crystallizing reagent. *Sov. Meteor. Hydrol.,* **5,** 33–45.

Kogan, Y., 1991: The simulation of a convective cloud in a 3D model with explicit microphysics. Part I: Model description and sensitivity experiments. *J. Atmos. Sci.,* **48,** 1160–1189.

Kovetz, A., and B. Olund, 1969: The effect of coalescence and condensation on rain formation in a cloud of finite vertical extent. *J. Atmos. Sci.,* **26,** 1060–1065.

Lew, J. K., and H. R. Pruppacher, 1983: A theoretical determination of the capture efficiency of small collumnar crystals by large cloud drops. *J. Atmos. Sci.,* **40,** 139–145.

——, D. E. Kingsmill, and D. C. Montague, 1985: A theoretical study of the collision efficiency of small planar ice crystals colliding with large supercooled water drops. *J. Atmos. Sci.,* **42,** 857–862.

——, D. C. Montague, and H. P. Pruppacher, 1986a: A wind tunnel investigation on the riming of snowflakes. Part I: Porous discs and large stellars. *J. Atmos. Sci.,* **43,** 2392–2409.

——, ——, and ——, 1986b: A wind tunnel investigation on the riming of snowflakes. Part 2: Nature and synthetic aggregates. *J. Atmos. Sci.,* **43,** 2410–2417.

Liu, Q., and Y. Kogan, 1998: Large eddy simulations of cloud processing of small size aerosols in marine stratocumulus. Preprints, *Conf. on Cloud Physics,* Everett, WA, Amer. Meteor. Soc., 329–332.

——, ——, and D. K. Lilly, 1995: Reducing the numerical dispersion of the cloud droplet spectrum in condensation calculations. Preprints, *Conf. on Cloud Physics,* Dallas, TX, Amer. Meteor. Soc., 112–117.

Low, T. B., and R. List, 1982: Collision, coalescence and breakup of raindrops. Part II: Parameterization of fragment size distributions. *J. Atmos. Sci.,* **39,** 1607–1618.

Lynn, B. H., A. P. Khain, J. Dudhia, D. Rosenfeld, A. Pokrovsky, and A. Seifert, 2005a: Spectral (bin) microphysics coupled with

a mesoscale model (MM5). Part I: Model description and first results. *Mon. Wea. Rev.,* in press.

——, ——, ——, ——, and ——, 2005b: Spectral (bin) microphysics with a mesoscale model (MM5). Part II: Simulation of a CAPE rain event with a squall line. *Mon. Wea. Rev.,* in press.

Magono, C., and C. Lee, 1966: Meteorological classification of natural snow crystals. *J. Fac. Sci. Hokkaido Univ. Ser. 7,* **2,** 321–362.

Maritinsson, B. C., and Coauthors, 1999: Droplet nucleation and growth in orographic clouds in relation to the aerosol population. *Atmos. Res.,* **50,** 289–315.

Mason, B. J., 1956: On the melting of hailstones. *Quart. J. Roy. Meteor. Soc.,* **82,** 209–216.

Matsuno, T., 1987: Effects of surface roughness and porosity on the riming of snowflakes. *J. Meteor. Soc. Japan,* **65,** 635–647.

Mazin, I. P., A. Kh. Krgian, and I. M. Imyanitov, 1989: *Handbook of Clouds and Cloudy Atmosphere.* Gidrometeoizdat, 647 pp.

Meyers, M. P., P. J. DeMott, and W. R. Cotton, 1992: New primary ice-nucleation parameterizations in an explicit cloud model. *J. Appl. Meteor.,* **31,** 708–721.

Mitra, S. K., O. Vohl, M. Ahr, and H. R. Pruppacher, 1990: A wind tunnel and theoretical study of the melting behavior of atmospheric ice particles. Part IV: Experiment and theory for snow flakes. *J. Atmos. Sci.,* **47,** 584–591.

Mossop, S. C., and J. Hallett, 1974: Ice crystal concentration in cumulus clouds: Influence of the drop spectrum. *Science,* **186,** 632–634.

Ovtchinnikov, M., and Y. L. Kogan, 2000: An investigation of ice production mechanisms using a 3D cloud model with detailed microphysics. Part I: Model description. *J. Atmos. Sci.,* **57,** 2989–3003.

——, ——, and A. M. Blyth, 2000: An investigation of ice production mechanisms using a 3D cloud model with detailed microphysics. Part II: Case study of New Mexico cumulus clouds. *J. Atmos. Sci.,* **57,** 3004–3021.

Phillips, V. T. J., T. W. Choularton, A. J. Illingworth, R. J. Hogan, and P. R. Field, 2003: Simulations of the glaciation of a frontal mixed-phase cloud with the Explicit Microphysics Model. *Quart. J. Roy. Meteor. Soc.,* **129,** 1351–1371.

Pinsky, M., and A. Khain, 1998: Some effects of cloud turbulence on water–ice and ice–ice collisions. *Atmos. Res.,* **47–48,** 69–86.

——, and ——, 2002: Effects of in-cloud nucleation and turbulence on droplet spectrum formation in cumulus clouds. *Quart. J. Roy. Meteor. Soc.,* **128,** 1–33.

——, ——, D. Rosenfeld, and A. Pokrovsky, 1998: Comparison of collision velocity differences of drops and graupel particles in a very turbulent cloud. *Atmos. Res.,* **49,** 99–113.

——, ——, and M. Shapiro, 1999: Collisions of small drops in a turbulent flow. Part I: Collision efficiency. Problem formulation and preliminary results. *J. Atmos. Sci.,* **56,** 2585–2600.

——, ——, and ——, 2000: Stochastic effects on cloud droplet hydrodynamic interaction in a turbulent flow. *Atmos. Res.,* **53,** 131–169.

——, ——, and ——, 2001: Collision efficiencies of drops in a wide range of Reynolds numbers: Effects of pressure. *J. Atmos. Sci.,* **58,** 742–764.

Pruppacher, H. R., and J. D. Klett, 1997: *Microphysics of Clouds and Precipitation.* 2d ed. Oxford University Press, 914 pp.

Rasmussen, R. M., and A. J. Heymsfield, 1987: Melting and shedding of graupel and hail. Part I: Model physics. *J. Atmos. Sci.,* **44,** 2754–2763.

——, V. Levizzani, and H. R. Pruppacher, 1984a: A wind tunnel and theoretical study of the melting behavior of atmospheric ice par-

ticles. II: A theoretical study for frozen drops of radius < 500 μm. *J. Atmos. Sci.,* **41,** 374–380.

——, ——, and ——, 1984b: A wind tunnel and theoretical study of the melting behavior of atmospheric ice particles. III: Experiment and theory for spherical ice particles of radius > 500 μm. *J. Atmos. Sci.,* **41,** 381–388.

——, I. Geresdi, G. Thompson, K. Manning, and E. Karplus, 2002: Freezing drizzle formation in stably stratified layer clouds: The role of radiative cooling of cloud droplets, cloud condensational nuclei, and ice initiation. *J. Atmos. Sci.,* **59,** 837–860.

Reisin, T., Z. Levin, and S. Tzvion, 1996a: Rain production in convective clouds as simulated in an axisymmetric model with detailed microphys. Part I: Description of the model. *J. Atmos. Sci.,* **53,** 497–519.

——, ——, and ——, 1996b: Rain production in convective clouds as simulated in an axisymmetric model with detailed microphysics. Part II: Effects of varying drops and ice initiation. *J. Atmos. Sci.,* **53,** 1815–1837.

——, S. Tzvion, and Z. Levin, 1996c: Seeding convective clouds with ice nuclei or hygroscopic particles: A numerical study using a model with detailed microphysics. *J. Appl. Meteor.,* **35,** 1416–1434.

Rosenfeld, D., 1999: TRMM observed first direct evidence of smoke from forest fires inhibiting rainfall. *Geophys. Res. Lett.,* **26,** 3105–3108.

——, 2000: Suppression of rain and snow by urban and industrial air pollution. *Science,* **287,** 1793–1796.

——, and W. L. Woodley, 1999: Satellite-inferred impact of aerosols on the microstructure of Thai convective clouds. *Proc. Seventh Scientific Conf. on Weather Modification,* Chiang Mai, Thailand, World Meteorological Organization, 17–20.

——, and ——, 2000: Deep convective clouds with sustained supercooled liquid water down to −37.5°C. *Nature,* **405,** 440–442.

Seifert, A., A. Khain, and U. Blahak, 2005: Possible effects of collisional breakup on mixed-phase deep convection simulated by a spectral (bin) cloud model. *J. Atmos. Sci.,* in press.

Stevens, B., G. Feingold, W. R. Cotton, and R. L. Walko, 1996: Elements of the microphysical structure of the numerically simulated nonprecipitating stratocumulus. *J. Atmos. Sci.,* **53,** 980–1006.

Takahashi, T., 1976: Hail in an axisymmetric cloud model. *J. Atmos. Sci.,* **33,** 1579–1601.

——, T. Endoh, and G. Wakahama, 1991: Vapor diffusional growth of free-falling snow crystals between −3° and −23°C. *J. Meteor. Soc. Japan,* **69,** 15–30.

Turpeinen, O., and M. K. Yau, 1981: Comparison of results from a three-dimensional cloud model with statistics of radar echoes on day 261 of GATE. *Mon. Wea. Rev.,* **109,** 1495–1511.

Tzvion, S., G. Feingold, and Z. Levin, 1989: The evolution of raindrop spectra. Part II: Collisional collection/breakup and evaporation in a rainshaft. *J. Atmos. Sci.,* **46,** 3312–3327.

Vali, G., 1975: Remarks on the mechanism of atmospheric ice nucleation. *Proceedings of the Eighth International Conference on Nucleation,* II. Gaivoronsky, Ed., Gidrometeoizdat, 265–269.

——, 1994: Freezing rate due to heterogeneous nucleation. *J. Atmos. Sci.,* **51,** 1843–1856.

Wang, P. K., and W. Ji, 1997: Numerical simulation of three-dimensional unsteady flow past ice crystals. *J. Atmos. Sci.,* **54,** 2261–2274.

Yin, Y., Z. Levin, T. Reisin, and S. Tzvion, 2000a: The effects of giant cloud condensational nuclei on the development of precipitation in convective clouds: A numerical study. *Atmos. Res.,* **53,** 91–116.

——, ——, ——, and ——, 2000b: Seeding convective clouds with hygroscopic flares: Numerical simulations using a cloud model with detailed microphysics. *J. Appl. Meteor.,* **39,** 1460–1472.